

Modeling, Dynamic Simulation, and Design of Magnetic Sensors Based On Magnetic Tunnel Junction Technology

by

Yu Ji

A thesis submitted to the Faculty of Graduate and Postdoctoral Affairs in partial fulfillment of the requirements for the degree of

Master of Applied Science

in

Mechanical Engineering

Carleton University
Ottawa, Ontario

© 2013, Yu Ji

Abstract

Spintronic devices, with the integration of magnetic materials and microstructures, have been enabling people to make use of the electron spin and charge properties in many applications. Few works, however, have been carried out thus far in modeling and simulation of these devices based on magnetic tunnel junction (MTJ) technology. Accordingly, this thesis proposes a novel modeling approach as well as an iterative simulation methodology for MTJs. A more comprehensive electrical tunneling model is established for better interpreting the conductance and current generated by the electron tunneling, and this model can also facilitate the iterative simulation of the micromagnetic dynamics. Given the improved tunneling model as well as the iterative dynamic simulation, the electric characteristics of an MTJ with an external magnetic field can be conveniently computed. Finally, the magnetic sensor design based on the MTJ technology and the fabrication methods are presented. These works would lay a useful foundation for the future development of new spintronic devices.

Acknowledgements

I would like to thank my thesis supervisor Professor Jie Liu for his enthusiastic supervision and patient guidance throughout this project. I would not have finished my thesis without his common sense, knowledge, perceptiveness and cracking-of-the-whip. Many thanks should also be given to Professor Junjie Gu and Mr. Richard Timmons (the President of Guildline Instruments Limited) for their insights and helpful suggestions during this work. I would like to acknowledge the help of Cameron Frazier; all the time, he is the right person I turn to for solving some problems in programming. In the meantime, I want to thank Professor Niall Tait and the technical officer Rob Vandusen for taking their time to answer my numerous questions in the microfabrication. Thanks are also due to Matteo Louter for our beneficial discussions.

I am grateful to all my friends in the Department of Mechanical and Aerospace Engineering, Carleton University, for their continued moral support and technical discussions during these two years of my graduate study.

Finally, the financial support from the Natural Sciences and Engineering Research Council of Canada (NSERC), and the Guildline Instruments Limited located at Smiths Falls, Ontario, Canada is greatly appreciated.

Table of Contents

Abstract.....	ii
Acknowledgements	iii
Table of Contents	iv
List of Tables	vii
List of Illustrations.....	viii
Nomenclature	xii
Chapter 1. Introduction.....	1
Chapter 2. Theoretical Background.....	6
2.1 Classification of Magnetic Materials	6
2.1.1 Diamagnetic	7
2.1.2 Paramagnetic.....	7
2.1.3 Ferromagnetic	8
2.1.4 Antiferromagnetic	9
2.1.5 Ferrimagnetic	10
2.2 Properties of Ferromagnetism	11
2.2.1 Magnetic Anisotropy	11
2.2.2 Demagnetizing Field.....	12
2.2.3 Exchange Interaction	13
2.2.4 Hysteresis Loop	13
2.3 Magnetoresistance.....	14
2.3.1 Anisotropic Magnetoresistance.....	14
2.3.2 Giant Magnetoresistance.....	15
2.3.3 Tunnel Magnetoresistance	16

2.4	Quantum Mechanics of the Tunneling Effect	20
2.4.1	One Dimensional Rectangular Barrier	21
2.4.2	One Dimensional Arbitrary Potential Barrier	25
Chapter 3.	MTJ Modeling and Simulation	28
3.1	Review of Tunneling Magnetoresistance Models	28
3.1.1	Jullière's Model	28
3.1.2	Slonczewski's Model	29
3.1.3	Simmon's and Brinkman's Model	33
3.2	Improved MTJ Electrical Tunneling Model	35
3.2.1	TMR Definition	35
3.2.2	Modified Conductance Model	36
3.3	Dynamic Magnetization in MTJ	39
3.3.1	The Calculation of Effective Field and Angle θ	39
3.3.2	Dynamic Magnetization Simulation	41
3.4	Simulation Result	46
3.4.1	Electrical Characteristic	47
3.4.2	Dynamic Simulation	50
Chapter 4.	Magnetic Sensor Design Based on MTJ	55
4.1	MTJ Sensor Design	55
4.2	The Function Descriptions of Each Layer	56
4.2.1	Substrate	56
4.2.2	Buffer Layer	56
4.2.3	Seed Layer	57
4.2.4	Antiferromagnetic Layer	57
4.2.5	Pinned Layer	58
4.2.6	Barrier Layer	59

4.2.7	Free layer	59
4.2.8	Capping Layer.....	60
4.3	MTJ Sensor Structure.....	60
4.4	MTJ Naming Conventions	62
4.5	Photoresist Masks.....	63
4.6	Alignment Marks	66
4.7	Fabrication Process	68
4.7.1	Equipment for Fabrication	68
4.7.2	Fabrication Process	78
4.7.3	Fabrication Plan	81
Chapter 5.	Conclusion and Future Works	83
5.1	Conclusions	83
5.2	Future Works.....	84
	Bibliography	85

List of Tables

Table 1	Parameters for tunneling electrical model	47
Table 2	Material properties in the dynamic magnetization simulation.....	52
Table 3	Exchange bias properties of spin-valve structures with different AF biasing layers [13].....	58
Table 4	Wafers of MTJs with different configurations	82

List of Illustrations

Figure 2.1	Diamagnetism phenomenon.	7
Figure 2.2	Paramagnetism phenomenon.	8
Figure 2.3	Ferromagnetism phenomenon.	9
Figure 2.4	Antiferromagnetism phenomenon.	10
Figure 2.5	Ferrimagnetism phenomenon.	11
Figure 2.6	Hysteresis loop of a ferromagnet starting from the origin.	14
Figure 2.7	The typical tri-layer structure of an MTJ.	17
Figure 2.8	Spin transfer schematic diagram: (a) The parallel configuration, (b) The antiparallel configuration.	20
Figure 2.9	The schematic of rectangular tunnel barrier.	21
Figure 2.10	The relationship between the transmission coefficient and the tunneling electron energy.	25
Figure 2.11	The schematic of the trapezoidal barrier with bias voltage V	26
Figure 3.1	TMR variation with increasing Fermi level polarization as defined by Jullière's and Slonczewski's model with a barrier height of 1.7eV; the barrier thicknesses for the calculation with Slonczewski's model are 0.5 nm, 1 nm, 2 nm, 10 nm, and 20 nm.	32
Figure 3.2	Rectified TMR versus bias voltage.	36
Figure 3.3	Directions of precession, damping and spin-transfer torque vectors in LLG model.	43

Figure 3.4	The generated tetrahedral mesh of an MTJ with 1 nm barrier layer by Netgen [33].....	44
Figure 3.5	The simulated electrical characteristics of the MTJ in both parallel and antiparallel configurations: (a) the G-V curve; (b) the I-V curve.....	48
Figure 3.6	Conductance comparison calculated from the Slonczewski's model, Brinkman's model and the improved electrical tunneling model with a barrier thickness of 1 nm and a barrier potential height of 1.7 eV.	49
Figure 3.7	The voltage-dependent current and conductance comparisons of the MTJ for different barrier thicknesses: (a) Current for thicknesses under 1.0 nm; (b) Current reversion phenomenon for large barrier thicknesses; (c) Conductance for thicknesses under 1 nm; and (d) Conductance reversion correspondingly for larger barrier thicknesses.	50
Figure 3.8	The trajectory of the magnetization of a cuboid based on LLG model: (a) Three-dimensional evolution of the magnetization vector; (b) Transient change of M_x , M_y and M_z within 1 ns.	51
Figure 3.9	The dynamic behavior of the free layer magnetization for an MTJ with 1 nm barrier: (a) $M_x - H$ curve; (b) $M_y - H$ curve.	53
Figure 3.10	The magnetic field dependence of the angle θ between the magnetizations of two FM layers and the current across the MTJ: (a) $\theta - H_x$ curve; (b) $I - H_x$ curve.	54
Figure 3.11	Resistance comparison of an MTJ from the experimental results reproduced from the literature [39] and the simulation result with the parameters from the experiment.	54

Figure 4.1	The schematic layout of the MTJ structure.	56
Figure 4.2	The electrode designs for the MTJs: (a)Bottom electrode design; (b)Top electrode design.	62
Figure 4.3	An example of the nomenclature of MTJ sensors.	63
Figure 4.4	Masks aligned together for photolithography.....	63
Figure 4.5	Mask 1: (a) Example of one block in Mask 1; (b) Zoomed in details of one cell with the bottom electrode shape in Mask 1.	65
Figure 4.6	Mask 2: (a) Example of one block in Mask 2; (b) Zoomed in details of one cell with the MTJ area of $16\mu\text{m} \times 16\mu\text{m}$ in Mask 2.	65
Figure 4.7	Mask 3: (a) Example of one block in Mask 3; (b) Zoomed in details of one cell with the exposure shapes for the bottom electrodes and the MTJ in Mask 3.	65
Figure 4.8	Mask 4: (a) Example of one block in Mask 4; (b) Zoomed in details of one cell with the shape of the top and bottom electrodes as well as the numbering marks in Mask 4.	66
Figure 4.9	Alignment marks for four layers: (a) All 4 alignment marks align together; (b-e) Alignment marks 1 to 4 are shown separately with the shades and the numbers.	67
Figure 4.10	BDF-4 furnace in CUMFF [52].....	70
Figure 4.11	Facilities for photo masks and photolithography [52]: (a) Heidelberg DWL-200 mask generator; (b) Karl-Suss MA-6 Aligner.	71
Figure 4.12	Fabricated photoresist mask 1: (a) The top side showing the mask patterns; (b) The bottom side showing the mask label.	72

Figure 4.13	Fabricated photoresist mask 2: (a) The top side showing the mask patterns; (b) The bottom side showing the mask label.	72
Figure 4.14	Fabricated photoresist mask 3: (a) The top side showing the mask patterns; (b) The bottom side showing the mask label.	73
Figure 4.15	Fabricated photoresist mask 4: (a) The top side showing the mask patterns; (b) The bottom side showing the mask label.	73
Figure 4.16	PlasmaTherm SLR-772 ECR RIE [53].	74
Figure 4.17	The Micro Magnetics SpinTherm 1000 Magnetic Thermal Annealing System [66].....	76
Figure 4.18	The Atomic Layer Deposition System: Oxford FlexALRPT [67].	78
Figure 4.19	Schematic diagram of the MTJ fabrication processes: (a) As-deposited film (simplified with the MTJ stack) after sputtering; (b) The first patterning and first etching step for bottom electrode; (c- d) After the second patterning and first etching step, the tunnel junction area is defined; (e) The insulator layer is deposited around the tunnel junction for separating the bottom and top electrodes; (f- k) After the exposure of the bottom electrode, the Ta bottom and top contact pads are defined.....	80
Figure 4.20	Three dimensional structure of a MTJ sensor after fabrication.....	81

Nomenclature

AMR	Anisotropic Magnetoresistance
AFM	Antiferromagnetic
ALD	Atomic Layer Deposition
CUMFF	Carleton University MicroFabrication Facility
CVD	Chemical Vapor Deposition
DC	Direct Current
DOS	Density of States
FM	Ferromagnetic
GMR	Giant Magnetoresistance
HDD	Hard Disk Drive
LLG	Landau–Lifshitz–Gilbert
MEMS	Microelectromechanical Systems
MR	Magnetoresistance
MRAM	Magnetoresistive Random-Access Memory
MTJ	Magnetic Tunnel Junction
NanoFab	Micro & Nanofabrication Facility
NIST	National Institute of Standards and Technology
PVD	Physical Vapor Deposition
RIE	Reactive Ion Etcher
RKKY	Ruderman-Kittel-Kasuya-Yosida
SAFM	Synthetic Antiferromagnetic
SI unit	International System of Units
STT	Spin-Transfer Torque
TMR	Tunnel Magnetoresistance
WKB	Wentzel–Kramers–Brillouin

Chapter 1. Introduction

Modern electrical technology is mostly dependent on the charge of electron. Electronics dominates human's life almost everywhere. Computers, city transportation systems and many other facilities will cease functioning without the use of electronics. However, another property of the electron is now increasingly attracting more attention. The spin of the electron, as its name suggests, can only point in one of the two directions, or quantum states (i.e., spin up and spin down), and this quantum phenomenon can thus be utilized in binary computer systems. Further exploration of this property leads to spintronics (i.e., spin transport electronics), which is an emerging technology exploiting both the intrinsic spin and the magnetic moment of the electron. In some special materials with an odd number of valence electrons, the magnetic moments from these unpaired valence electrons can display a measurable magnetic field macroscopically when they are aligned along the same direction without an external magnetic field. This phenomenon is named as ferromagnetism with its property deriving from the direct influence of two quantum mechanical effects: spin and the Pauli Exclusion Principle [1].

Ferromagnetic (FM) materials exhibit a phenomenon of magnetoresistance (MR), which corresponds to the change in resistance of the material due to an externally applied magnetic field. The MR ratio, defined as the resistance change under an external magnetic field between the two saturated states, divided by the minimal resistance in the parallel state, describes the performance of FM materials. The higher the MR value is, the higher the resistance to field sensitivity will be. The anisotropic magnetoresistance

(AMR) in Iron-Cobalt-Nickel based materials is the first MR effect discovered by William Thompson in 1857 [2]. It was not until a century later, in the 1970s, when the AMR was found to show a few percent change in resistance at the room temperature, that the AMR was exploited commercially for hard disk drives (HDD) [3]. With the growing demands for higher HDD storage density, other forms of MRs with larger variances of resistance due to applied external magnetic fields were discovered. Two main forms of MRs are: giant magnetoresistance (GMR) and tunnel magnetoresistance (TMR). GMR was discovered in 1988, which brought the 2007 Nobel Prize in Physics to the two scientists who had discovered it [4]. It is also interesting to know that one of these two scientists, Peter Andreas Grunberg did his postdoctoral research at Carleton University from 1969 to 1972. The main applications of the GMR lie in HDDs, biosensors, microelectronic mechanical systems (MEMS), magnetoresistive random-access memories (MRAMs), and many other devices.

The TMR is similar to GMR in principle, but the quantum mechanical coherence effects associated with the TMR allow electrons to tunnel through the barrier, which greatly enhances its MR compared to that of GMR. The devices exhibiting the TMR effect are called magnetic tunnel junctions (MTJs) and their TMR model was first built by Jullière, demonstrating the spin polarized tunneling phenomenon between two metals separated by an insulator in 1975 [5]. The TMR, defined as the total change in the resistances of an MTJ device between two saturated configurations divided by its lowest resistance in parallel configuration, is therefore an important physical parameter for evaluating the MTJ's response to an external magnetic field.

MTJs with aluminum oxide (Al_2O_3) barrier were discovered and used since the 1990s, with MR values up to 70%. However, later research on MTJs with magnesium oxide (MgO) barrier demonstrated that this kind of MTJs could generate MR values up to 1000% theoretically [6]. This theoretical finding was validated by the subsequent experimental work done in 2008 in which it was reported that MTJs with MgO barrier could offer a MR as high as 604%, far surpassing the amorphous AlO_x [8]. These research works brought MTJs to be among the most promising technologies for sensor development for room-temperature applications.

The two main applications of MTJs are memory storing (e.g., HDD and MRAM) and high-resolution magnetic field sensors thanks to their smaller size, lower cost as well as lower energy consumption compared to traditional magnetic sensors. On one hand, the high sensing ability with high signal-to-noise ratio of MTJs makes them ideal candidates for high density HDD read/write heads. On the other hand, MTJs also exhibit large resistance changes between two saturated states representing “0” and “1”, which leads to their ideal application of MRAM storage. Meanwhile, MTJs can also exhibit a semi-linear response to external magnetic fields, which can be potentially utilized for sensor development for low magnetic field sensing.

This thesis will discuss both the theoretical modeling and dynamic simulation of MTJs, as well as the design of magnetic sensors based on MTJ technology. The target system in this work will be $\text{Co}_{40}\text{Fe}_{40}\text{B}_{20} / \text{Al}_2\text{O}_3 / \text{Co}_{40}\text{Fe}_{40}\text{B}_{20}$ MTJ. The rest of this thesis will be organized as follows.

Chapter 2 gives some theoretical background for understanding this thesis. It begins with the physics of magnetism, including a discussion of the magnetic material classification and the properties of FM materials. Different types of MR devices will then be introduced, with an emphasis on the TMR. This chapter will also discuss the quantum tunneling mechanism of the MTJ with first, a simple one-dimensional rectangular potential barrier and then a more complicated barrier with an arbitrary potential height.

In Chapter 3, the modeling and dynamic simulation of MTJs will be described. This begins with a brief review of TMR models from previous works. Each of the relevant models has its own advantages and limitations, and none of them can be independently employed to reliably describe the behavior of MTJs. An improved electrical TMR tunneling model is therefore proposed for a more accurate voltage-dependent conductance calculation. The magnetization angle of the two FM layers is critical to the tunneling current calculation, which is solved by dynamic magnetization simulation proposed in this work. The simulation results of the magnetization variation and the resultant current flowing through the simulated MTJ will be given and discussed as well.

In Chapter 4, a magnetic sensor design based on the MTJ technology will be presented. The designed MTJ sensor possesses the $\text{Co}_{40}\text{Fe}_{40}\text{B}_{20}/\text{Al}_2\text{O}_3/\text{Co}_{40}\text{Fe}_{40}\text{B}_{20}$ MTJ structure whose TMR and magnetic sensitivity could be potentially improved by several other auxiliary layers. The functionality for each layer will be discussed. The photoresist masks for patterning the designed MTJ have been produced. The fabrication process and the relevant equipment will be presented as well.

Finally, the conclusion remarks and some future research topics are summarized in Chapter 5.

Chapter 2. Theoretical Background

In this chapter, the background of magnetic materials and their relevant mechanism will be described. The focus is placed on the properties of FM materials and the TMR effect. The quantum mechanical tunneling effect is elaborated using a rectangular barrier and an arbitrary barrier for the MTJ.

2.1 Classification of Magnetic Materials

The classification of magnetic materials is based on their response to an externally applied magnetic field, which is revealed by the permeability and susceptibility of the materials. For a magnetic material, the magnetic susceptibility χ is defined as the ratio of the magnetization M over the applied magnetic field H , which describes the response in the material magnetization to the applied magnetic field. Permeability μ is defined as the ratio of the magnetic induction B over the applied magnetic field H , which reveals the ability of a magnetic material to support the formation of the magnetic field within itself. For simplicity the relative permeability μ_r is commonly used in physics, which is the ratio of the permeability of a specific medium to the permeability of free space.

Magnetic materials with a negative susceptibility are called diamagnets whereas magnetic materials with a positive susceptibility are named as paramagnets. Strong coupling between dipole moments in magnetic materials results in several kinds of magnetic substance, and each of them has different magnetic characteristics.

2.1.1 Diamagnetic

The diamagnetism is a weak form of magnetism, which is mainly attributed to the orbital motion of electrons that creates a magnetic moment m . According to the Lenz's law, the individual magnetic moments in a diamagnetic material are magnetized in the opposite polarity under the application of an external magnetic field and are therefore repelled by the field, counteracting the change in the applied field. This results in a magnetization in the opposite direction of the applied field. Such materials have a negative and very weak relative susceptibility ($\sim -10^{-5}$), and the relative permeability is usually less than 1. In the absence of the external magnetic field, the individual moments of the atoms in the diamagnet do not exhibit a magnetization, such that the total magnetization is null.

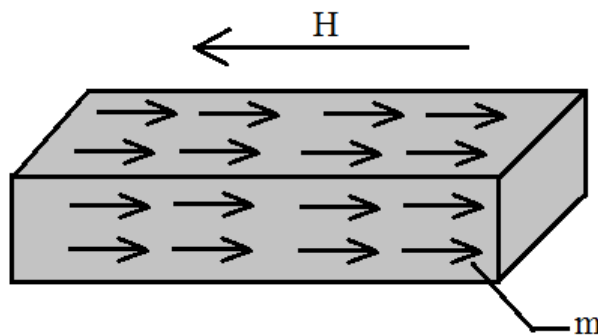


Figure 2.1 Diamagnetism phenomenon.

2.1.2 Paramagnetic

The total magnetization of paramagnetic materials also stays null in the absence of the external magnetic field, with randomly oriented magnetic moments of atoms in the materials. But in the presence of an external magnetic field, each individual magnetic moment will align along the direction of the field, resulting in a parallel magnetization

proportional to the magnetic field. However these materials are still weakly attracted towards magnetic field. Typically, the relative permeability of such materials is slightly bigger than 1, which is independent of magnetic field strength and is inversely proportional to temperature. Meanwhile, the relative susceptibility of paramagnetic materials ($\sim 10^{-3} - 10^{-5}$) is also inversely proportional to the absolute temperature, known as the Curie-Weiss law.

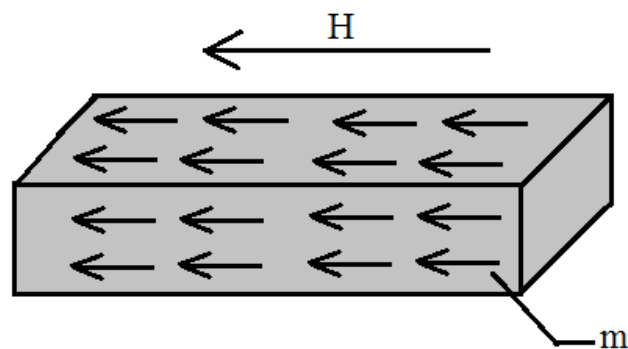


Figure 2.2 Paramagnetism phenomenon.

2.1.3 Ferromagnetic

The FM material can present a net magnetization, even in the absence of an external magnetic field. In the presence of a magnetic field, each individual magnetic moment tends to align parallel to the applied field and a net magnetization can be observed. Most ferromagnets are 3d transition metals or their alloys as the 3d band in these elements is empty and therefore exhibit a permanent spin and an orbital moment (i.e., spontaneous magnetic moment). Their permeability depends not only on the magnetic field strength but also on their magnetization history, which means that their magnetizations are non-stationary, leading to a hysteresis loop in the H-M curve. A typical ferromagnet can exhibit a large susceptibility to the order of 10^6 , compared to other types of magnetic

materials, which makes it much easier to be magnetized. As the external magnetic field strength increases, ferromagnets will reach their magnetic saturation, such that ferromagnets can only be magnetized to a certain limit.

The two important properties of FM materials include the Curie temperature and their magnetic domains. The magnetization of FM materials will disappear and become paramagnetic above a certain temperature, known as the Curie temperature T_c . Below the Curie temperature, the magnetization of the FM material will be spontaneously divided into many small regions, known as the magnetic domains. The magnetization within each domain points in a uniform direction, but the magnetization of different domains may point in different directions. Such magnetic domains are formed in the FM materials to minimize its internal energy.

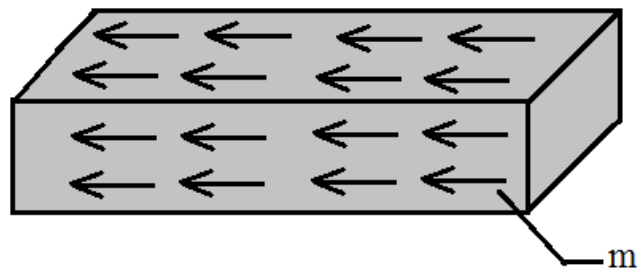


Figure 2.3 Ferromagnetism phenomenon.

2.1.4 Antiferromagnetic

In antiferromagnetic (AFM) materials, the magnetic moments of atoms in each lattice layer are aligned antiparallely due to the exchange interaction forces, such that the magnetization remains null in the absence of the external magnetic field. Antiferromagnets usually have low permeabilities and low but positive susceptibilities,

which vary with the temperature in the same way as the paramagnets. This temperature-dependent characteristic is only valid under a certain temperature, known as the Néel temperature, θ_N . When the temperature increases to or above the Néel temperature, the magnetic moments will become randomly oriented and the susceptibility will decrease. As a result, the AFM arrangement of the magnetic moments vanishes, and the materials become paramagnetic.

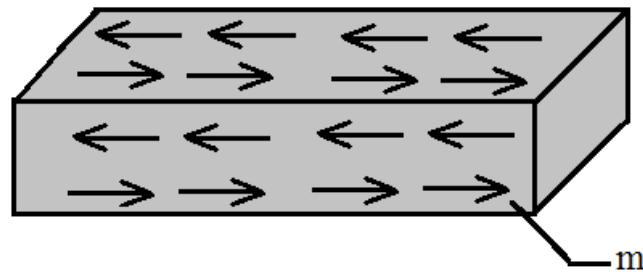


Figure 2.4 Antiferromagnetism phenomenon.

2.1.5 Ferrimagnetic

Ferrimagnetism is similar to both ferromagnetism and antiferromagnetism in some way. The ferrimagnetic materials exhibit a spontaneous magnetization below the Curie temperature T_c . When temperature increases and passes the temperature T_c , the magnetic moment arrangement inside the ferrimagnet is disturbed, resulting in random orientations of magnetic moments and the ferrimagnet becomes paramagnetic. Meanwhile, the ferrimagnetic materials also possess some characteristics of antiferromagnetic materials in that the magnetic moments of adjacent ions on different sub-lattices are opposite in direction due to the exchange coupling. As a result, the spontaneous magnetization of the ferrimagnetic materials is not null due to unequal magnetic moments along these two directions (Figure 2.5).

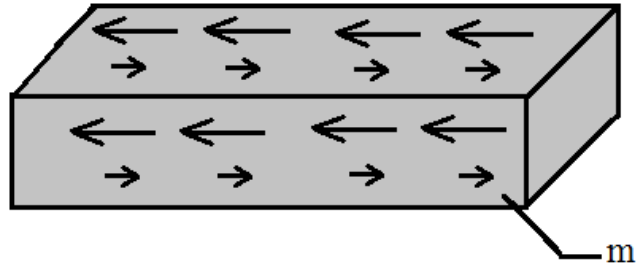


Figure 2.5 Ferrimagnetism phenomenon.

2.2 Properties of Ferromagnetism

2.2.1 Magnetic Anisotropy

The magnetic anisotropy is the directional preference of the magnetic moments in magnetic materials, which is responsible for the self-alignment of the spontaneous magnetization along a particular direction that is termed as the easy axis. The two opposite directions along the easy axis are equivalent and the magnetization of the material can be along either of them due to the spontaneous symmetry breaking effect [57].

There are a variety of sources for the magnetic anisotropy property [58], including the magnetocrystalline anisotropy due to different magnetic behavior along different crystallographic directions in polycrystalline, the shape anisotropy due to the asymmetry of the demagnetizing field when the material shape is not perfectly spherical, the magnetoelastic anisotropy due to the tension variation, and the exchange anisotropy due to the interaction between the AFM and FM materials.

For most spintronic devices, the magnetic materials are generally monodomain [13], leading to the uniformity and unison of the magnetization inside the magnetic materials., As a result, the variety of the direction dependence of the magnetic anisotropy on the components of unit magnetization vectors in such materials leads to several kinds of magnetic anisotropies, such as the uniaxial magnetic anisotropy, the triaxial magnetic anisotropy, and the cubic magnetic anisotropy.

2.2.2 Demagnetizing Field

The demagnetizing field, also known as stray field, is the magnetic field generated by the magnetization of the magnetic material, which orients toward the opposite direction of the magnetization and reflects the tendency to reduce the total magnetic moment. It gives rise to the shape anisotropy in monodomain FM materials. The magnetoelastic energy associated with the demagnetizing field is dependent on the distance of the magnetic poles and, tends to be minimized, resulting in the division of the magnetic domains.

The calculation of the demagnetization field is not a trivial work even for a uniform magnetization. It is generally taken into account in the calculation of the effective magnetic field by a geometry-dependent constant called demagnetizing factor, which will be discussed in section 3.3.1.

2.2.3 Exchange Interaction

In MTJs, the exchange coupling takes place between the AFM and the FM materials close to it. It is a very strong but short range effect and is independent of the directions of the total magnetic moment and the external magnetic field. When a layer of FM material and a layer of AFM material are in contact or separated by a very thin non-magnetic spacer, the interaction between these two materials forces the magnetic dipole of an atom to align with the magnetic dipole of its neighbor, resulting in a smooth dipole orientation, and the dipoles of the atoms at the interface lattice layers of these two materials are aligned antiparallel. Since the AFM materials exhibit no total magnetization, the magnetization direction of the FM material is considered to be fixed by the AFM layer.

2.2.4 Hysteresis Loop

When an external magnetic field is applied to a ferromagnet, the atomic dipoles tend to align with it, but the relationship between the field strength H and the magnetization M is not linear. When H increases from the origin, M follows the curve called the initial magnetization curve and finally approaches the saturation magnetization M_s . When H decreases from this point, M will not follow the initial magnetization curve. Instead, there exists a remnant magnetization M_r when H decreases to zero. M can be brought back to zero when a magnetic field in the opposite direction is exerted on the material, which is known as the coercive field H_c . If the $H - M$ relationship is plotted within a period of the applied magnetic field, the hysteresis loop will be formed and a schematic of the hysteresis loop in a FM material is shown in Figure 2.6.

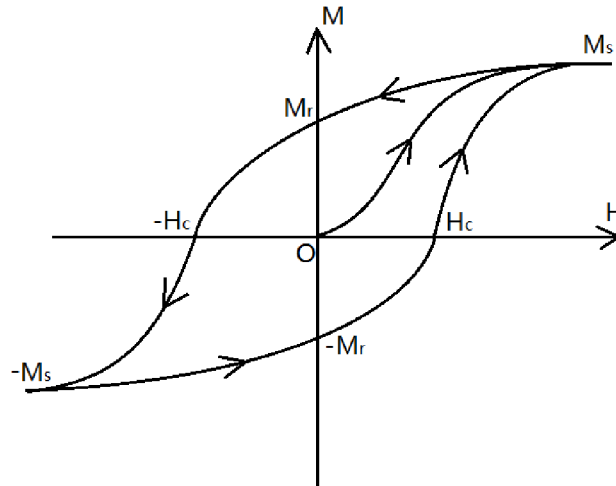


Figure 2.6 Hysteresis loop of a ferromagnet starting from the origin.

2.3 Magnetoresistance

MR reveals the change in the resistivity of a magnetoresistive material due to the externally applied magnetic field. The first MR effect, known as AMR, was discovered in 1857 [2]. Other forms of MR were then discovered with higher resistance changes in the past decades, and among them two MRs are critical, known as GMR and TMR. For magnetic field sensing applications, a higher MR is usually desired.

2.3.1 Anisotropic Magnetoresistance

The AMR is tied to the anisotropic scattering of electrons that is caused by the spin-orbit interaction between the current density and the applied magnetic field, such that the resistance of a material changes sinusoidally with the direction of the applied magnetic field. An AMR device reaches its maximum resistance when the electrical current aligns parallel with the magnetic field, and its minimum resistance when the electrical current is perpendicular to the direction of the magnetic field.

The AMR is given as a function of the resistances in parallel and perpendicular configuration:

$$\text{AMR} = \frac{R_{\parallel} - R_{\perp}}{\frac{1}{3}R_{\parallel} + \frac{2}{3}R_{\perp}} \times 100\%, \quad (1)$$

where R_{\parallel} (or R_{\perp}) are the resistances in a magnetic field parallel (or perpendicular) to the current direction.

AMR has been exploited in a variety of magnetic sensing applications. The high sensitivity to the change of the magnetic field enables its applications in measuring the Earth's magnetic field, the electromagnetic field around the conductor, the linear position and angular location, and so on.

2.3.2 Giant Magnetoresistance

GMR was discovered by Albert Fert and Peter Grunberg independently in 1988, which brought them the Nobel Prize in physics in 2007 [4]. It was observed in a thin-film multilayer structure composed of two FM conducting layers separated by a non-magnetic conductive material: Fe/Cr/Fe. The resistance of the GMR structure changes with the magnetization directions of the two FM layers. When a current passes through the GMR, the scattering effect occurs corresponding to the FM layer, which leads to the spin-polarizations of the current. When the two FM layers are aligned parallel, spin-polarized current can easily pass through both of them, resulting in a low overall resistance; when the two FM layers are aligned antiparallel, the spin-polarized current will only pass

through the FM layer with the same polarization easily, thereby resulting in a high overall resistance.

The GMR can be defined as the difference between the resistances in parallel and antiparallel states normalized by the resistance in parallel state:

$$\text{GMR} = \frac{R_{\text{AP}} - R_{\text{P}}}{R_{\text{P}}} \times 100\%, \quad (2)$$

where the subscripts refer to the parallel and antiparallel configurations of the magnetizations of these two FM layers, respectively. The values of GMR turn out to be higher than those of AMR, endowing their better performance in magnetic field sensing applications (e.g., HDDs and biosensors).

2.3.3 Tunnel Magnetoresistance

A typical MTJ is of a tri-layer structure consisting of two FM layers sandwiching an ultra-thin insulator film (i.e., the barrier layer) that is usually a few nanometers thick. One of the FM layers is pinned (i.e., the pinned layer) in its magnetization direction, whereas the other layer is left free (i.e., the free layer) to respond to the external magnetic field. When the magnetizations of both FM layers are aligned (i.e., the parallel configuration), the MTJ reaches its highest conductance (i.e., the lowest resistance), and on the contrary, when the magnetizations of both FM layers are anti-aligned (i.e., the antiparallel configuration), the MTJ reaches its lowest conductance (i.e., the highest resistance). The magnetization of the pinned layer can be achieved and maintained by making use of the exchange coupling effect from a neighboring AFM layer (i.e., an extra layer) [9]. As a result, the magnetization of the pinned layer will not vary with the change of the applied

magnetic field due to its high coercivity, whereas the free layer will respond to the applied field due to its low coercivity [10]. The TMR, defined as the total change in resistance between these two configurations divided by the lowest (i.e., the parallel-state) resistance, is therefore often employed as an important physical parameter for evaluating MTJ's sensitivity in response to an external magnetic field. A typical structure of the MTJ with the antiparallel configuration is shown in Figure 2.7 in which the arrows indicate the magnetization orientations of the FM layers.

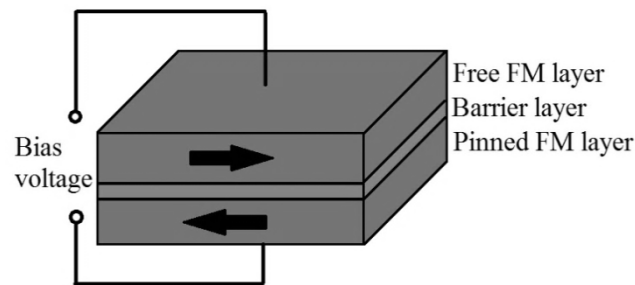


Figure 2.7 The typical tri-layer structure of an MTJ.

Classical physics predict that there should be no current flowing through the insulating barrier when a voltage is applied to the FM electrodes on both sides of an MTJ. However, when the insulating barrier is ultra-thin (e.g., a few nanometers), a quantum tunneling effect may take place in the MTJ, which allows electrons to transfer from one FM layer to the other. An MTJ with a bias voltage may therefore exhibit electrical conducting properties and its electrical resistance varies as a function of the magnetic field strength over a certain field range. For HDD and MRAM applications, the resistance will switch between these two saturated states to represent digital bits “1” or “0”; whereas for low-

field sensing applications, the orientation of magnetization of the free layer will vary with respect to the external magnetic field of interest.

The MTJ is an MR device. Such devices are often compared using MR ratio as an essential figure of merit, and the higher MR ratio usually means the higher sensitivity to the variation of the external magnetic field. The TMR is defined as:

$$TMR = \frac{R_{AP} - R_P}{R_P} = \frac{G_P - G_{AP}}{G_{AP}}, \quad (3)$$

where R_P and G_P are respectively the resistance and the conductance in parallel configuration; R_{AP} and G_{AP} are respectively the resistance and the conductance in antiparallel configuration. In addition the mean conductance for an MTJ can be calculated as $\bar{G} = (G_P + G_{AP}/2)$.

An electron in the FM layers only has two spin directions based on the magnetization of the FM layer containing this electron: either spin-up or spin-down. In this work, it is assumed that there is no spin-flip scattering, which may be caused by the impurity of the barrier material [65], when the electrons tunnel through the barrier; instead the electrons in one FM electrode will tunnel through the barrier layer to the other electrode while staying in their original spin directions. Under such consumption, if the spin-up electrons occupy the majority of the electron population in one electrode, the tunneled spin-up electrons will also occupy the majority in the other electrode when the FM layers are in parallel configuration. In the case that the FM layers are in antiparallel configuration, the

tunneled spin-up electrons will, however, occupy the minority of the electron population in the other electrode.

The relative spin direction of an electron is determined by the magnetization of the electrode. Since there is no spin flip for the tunneled electrons, the relative spin direction of tunneled electrons in parallel configuration stays the same in both electrodes, whereas the relative spin direction of the electron will flip in antiparallel configuration. As a result, the conduction through the barrier can be divided into two channels for these two relative spin directions based on Mott's method [11], and the conductance for parallel and antiparallel states can then be given as:

$$G_P = G_{\uparrow\uparrow} + G_{\downarrow\downarrow}, \quad (4)$$

$$G_{AP} = G_{\downarrow\uparrow} + G_{\uparrow\downarrow}, \quad (5)$$

where $\uparrow\uparrow$ means the relatively spin-up electrons stay spin-up after tunneling through the barrier, $\downarrow\downarrow$ means the relatively spin-down electrons stay spin-down after tunneling through the barrier, $\uparrow\downarrow$ means the relatively spin-up electrons become spin-down after tunneling through the barrier, and $\downarrow\uparrow$ means the relatively spin-down electrons become spin-up after tunneling through the barrier. Figure 2.8 shows the spin transfer process in an MTJ with two spin transfer channels.

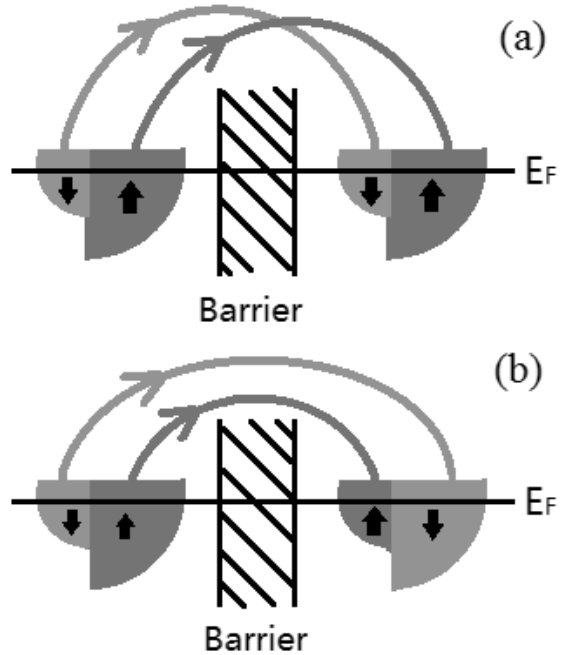


Figure 2.8 Spin transfer schematic diagram: (a) The parallel configuration, (b) The antiparallel configuration.

The mean conductance of an MTJ can then be further expressed as:

$$\bar{G} = \frac{G_{\uparrow\uparrow} + G_{\downarrow\downarrow} + G_{\uparrow\downarrow} + G_{\downarrow\uparrow}}{2}. \quad (6)$$

Equation (6) will be employed to conveniently calculate the mean conductance of the MTJ of interest at zero bias in Chapter 3.

2.4 Quantum Mechanics of the Tunneling Effect

For devices on a nanometer scale, classical physics usually cannot explain the transmission phenomenon of electrons through an insulating barrier with a higher potential energy than the kinetic energy of the tunneling electrons, and in this case the Heisenberg's uncertainty principle takes place. The mechanism of the MTJs is essentially the quantum tunneling of electrons and is therefore necessary to be explained by quantum

mechanism. The tunneling effect of the electrons in MTJs will be explained using an ideal one dimensional rectangular potential barrier and an arbitrary potential barrier. The Schrödinger's wave function will be employed for describing the behavior of the tunneling electrons.

2.4.1 One Dimensional Rectangular Barrier

To illustrate the wave-mechanical transportation of electrons through an insulating barrier between two conducting metals, a one-dimensional barrier is given in Figure 2.9 with several assumptions such as identical metal electrodes, perfect interfaces, elastic interactions and negligible image potentials [18]. The two metal electrodes have a potential energy $U(x)$ at the region I and region III, and the barrier has a potential energy U_0 within the region II ($0 \leq x \leq a$). When an electron with kinetic energy E encounters the barrier from the region I, it can be either transmitted or reflected by the barrier.

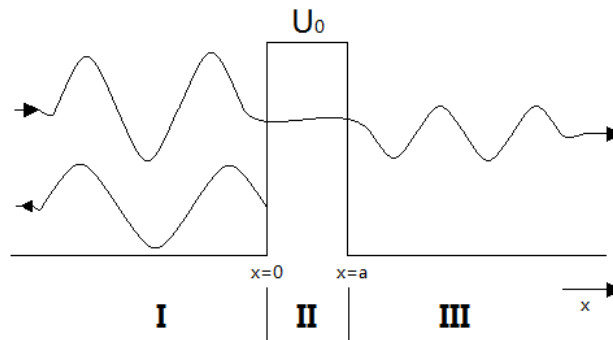


Figure 2.9 The schematic of rectangular tunnel barrier.

Based on the classical physics, if E is lower than U_0 , the electron will be reflected by the barrier; otherwise it will transmit through the barrier from region I to region III.

However, quantum mechanism suggests that even in this case both reflection and transmission are possible with a probability. The wave function $\psi(x)$ and the likelihood of transmission (i.e., the transmission coefficient) can be calculated using the Schrödinger's wave function:

$$E\psi(x) = \left[-\frac{\hbar}{2m} \nabla^2 + U_0 \right] \psi(x), \quad (7)$$

where $\hbar = h/2\pi$ is the reduced Planck constant or Dirac constant, h is the Planck constant, $\Psi(x)$ is the wave function, ∇^2 is the Laplacian operator (i.e., the second order derivative of $\Psi(x)$), and m is the mass of the particle (i.e., the electron mass in this case).

Since the potential is constant in all the regions, the electron can be considered as in a quasi-free state. In region I, there is no potential acting on the incident electrons and the electron wave function consists of the incident wave function moving towards region II and the reflected wave function in the opposite direction from the interface of region I and II (i.e., $x=0$). In region II, the wave function consists of the transmitted wave function through the potential barrier and the reflected wave function from the interface of region II and III (i.e., $x=a$). It is supposed that there are only transmitted electrons in region III, and no potential acts on the electrons in this region. The solution, known as the Schrödinger's wave equation, can be written as a superposition of moving waves in two directions:

$$\psi(x) = \begin{cases} A\exp(ik_1x) + B\exp(-ik_1x) & x \leq 0 \\ C\exp(ik_2x) + D\exp(-ik_2x) & 0 \leq x \leq a, \\ E\exp(ik_1x) & x \geq 0 \end{cases} \quad (8)$$

where A-E denotes the direction of the velocity vectors and k_1, k_2 are defined as:

$$k_1 = \frac{\sqrt{2mE}}{\hbar}, \quad k_2 = \frac{\sqrt{2m(U_0 - E)}}{\hbar}. \quad (9)$$

It is assumed that the wave function and its first-order derivatives are continuous everywhere along the interfaces of the potential barrier and the two electrodes (i.e., at $x=0$ and $x=a$), and the resultant relations for the coefficients in the wave function are given by:

$$\begin{cases} A + B = C + D \\ (A - B)ik_1 = (C - D)ik_2 \\ C\exp(ik_2a) + D\exp(-ik_2a) = E\exp(ik_1a) \\ C ik_2 \exp(ik_2a) - D ik_2 \exp(-ik_2a) = E ik_1 \exp(ik_1a) \end{cases}. \quad (10)$$

The transmission coefficient T is defined as the ratio of the transmitted current density over the incident current density:

$$T = \frac{v_{III}E \times E}{v_I A \times A}, \quad (11)$$

where v_I and v_{III} are the group velocities of electrons in region I and III and are numerically equivalent since the effective mass and momentum of electrons remains unchanged in the barrier. Similarly, the reflection coefficient can be defined as:

$$R = \frac{v_I B \times B}{v_I A \times A}. \quad (12)$$

By substituting the expressions for the coefficients A , B and E , the transmission coefficient and the reflection coefficient are given as:

$$T = \left[\frac{E}{A} \right]^2 = \left[1 + \frac{\sinh^2(k_2a)}{4 \frac{E}{U_0} \left(1 - \frac{E}{U_0} \right)} \right]^{-1}, \quad (13)$$

$$R = \left[\frac{B}{A} \right]^2 = \left[1 + \frac{4 \frac{E}{U_0} \left(1 - \frac{E}{U_0} \right)}{\sinh^2(k_2 a)} \right]^{-1}. \quad (14)$$

The sum of the transmission coefficient and the reflection coefficient is 1 (i.e., the sum of the possibilities of both transmitted and reflected electrons). It is noted that when $k_2 a$ is much larger than 1 (i.e., $k_2 a \gg 1$), the transmission coefficient becomes quite small, and can therefore be approximated as:

$$T \approx \frac{16E(U_0 - E)}{U_0^2} \exp(-2k_2 a). \quad (15)$$

Figure 2.10 shows the transmission probability of electrons tunneling through a potential barrier with a thickness of 1nm, and a potential height of 1.7eV. The dashed line is the result in classical physics with only two states (i.e., 0% and 100%) for electrons with different energies. However in quantum mechanics, the transmission coefficient is a very small finite number when $E < U_0$; this coefficient quickly increases and approaches to 1 with certain fluctuations when $E > U_0$. A special case is that when $E = U_0$, the transmission coefficient is given as:

$$T = \frac{1}{1 + \frac{2ma^2 U_0}{\hbar^2}}. \quad (16)$$

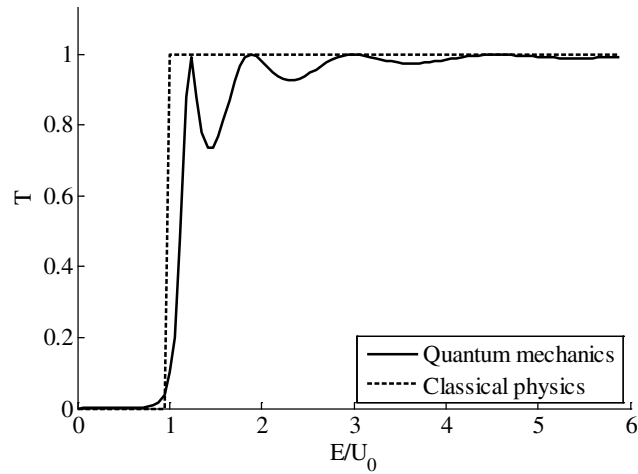


Figure 2.10 The relationship between the transmission coefficient and the tunneling electron energy.

2.4.2 One Dimensional Arbitrary Potential Barrier

The expression in the previous section can ideally describe the transmission behavior of electrons tunneling through a rectangular barrier, which is however not practical as the rectangular barrier is only an ideal system with a constant potential height. For a tunneling junction with different electrodes and a bias voltage, the potential energy across the structure will be asymmetric, and can be expressed as $U(x, V)$ that is a function of the distance and the applied voltage. The bias voltage shows a potential incensement $e \cdot V$ in region I over region III, and the potential barrier in region II turn to be trapezoidal as is shown in Figure 2.11.

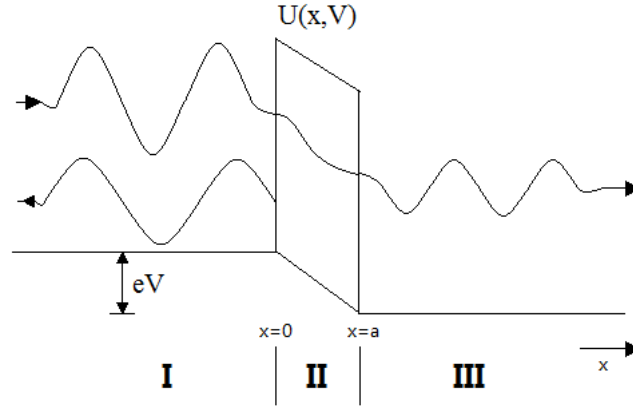


Figure 2.11 The schematic of the trapezoidal barrier with bias voltage V .

To better describe such potential barriers, Wentzel-Kramers-Brillouin (WKB) method can be applied to approximate the transmission coefficient [59]. This method considers the potential change in the barrier. It solves the Schrödinger wave function with breakdowns at the turning points of the electron energy so as to generate a continuous wave function [60].

The Schrödinger wave function $\psi(x)$ is expressed as:

$$\frac{d^2\psi(x)}{dx^2} = \frac{2m}{\hbar^2} (U(x, V) - E)\psi(x). \quad (17)$$

If the wave function $\psi(x)$ is expressed as the exponential form of another function $\phi(x)$:

$$\psi(x) = e^{\phi(x)}. \quad (18)$$

Equation (17) can be rewritten as a function of the first and second order derivative of the function ϕ with respect to x :

$$\phi''(x) + \phi'^2(x) = \frac{2m}{\hbar^2} (U(x, V) - E). \quad (19)$$

By solving this equation with the first order expansion of the real and image part of $\phi'(x)$ and some mathematical manipulations, the Schrödinger wave function $\psi(x)$ for the case that the barrier potential is higher than the electron energy is given as [61]:

$$\psi(x) \approx \frac{C_+ e^{\int \sqrt{\frac{2m}{\hbar^2}(U(x,V)-E)} dx} + C_- e^{-\int \sqrt{\frac{2m}{\hbar^2}(U(x,V)-E)} dx}}{\sqrt[4]{\frac{2m}{\hbar^2}(U(x,V) - E)}}, \quad (20)$$

where C_+ and C_- are constants relating with the barrier potential and the electron energy.

The WKB approximates the Schrödinger equation when the potential varies slowly in the region II such that the tunneling electrons are considered to be approximately constant over many wavelengths [63]. However, it is not valid near the classical turning point (i.e., $E = U(x,V)$) where the WKB approximation solution become singular and the wave function solution can either be oscillating or undergoing exponential amplitude shifting. The solution near the turning point, where $E = U(x,V)$, is yet to be found, but a differential equation known as the Airy function can be applied to locally solve this problem [62].

Chapter 3. MTJ Modeling and Simulation

Much research efforts have thus far been taken to model the electron quantum tunneling effect. Among them, four modeling approaches have made significant contributions towards the development of the MTJ. These models and their respective limitations will be briefly discussed and the terminologies involved will be used in the presentation of the proposed modeling approach for the sakes of consistency and readability. The proposed electrical tunneling model endeavors to address all the influences from the bias voltage, the applied voltage, the external field, and the magnetization configuration, as well as the effects of the relevant key junction physical parameters, and is capable of providing more accurate interpretations for the electrical characteristics of the MTJ. Finally the dynamic simulation proposed in this chapter is achieved by implementing the LLG equation in the finite element analysis, and the simulation results can facilitate the interpretation of the effective magnetic field, the magnetization angle for FM electrodes, and the micromagnetic behaviors.

3.1 Review of Tunneling Magnetoresistance Models

3.1.1 Jullière's Model

Jullière established the first model for MTJs, in which it is stated that the tunneling current density is proportional to the sum of current densities in each spin channel in the electrode [5]. The current density for each channel is the product of electron densities of states (DOS) for electrons in both electrodes:

$$J_P \propto J_{\uparrow\uparrow} + J_{\downarrow\downarrow} = \rho_{1\uparrow}\rho_{2\uparrow} + \rho_{1\downarrow}\rho_{2\downarrow}, \quad (21)$$

$$J_{AP} \propto J_{\uparrow\downarrow} + J_{\downarrow\uparrow} = \rho_{1\uparrow}\rho_{2\downarrow} + \rho_{1\downarrow}\rho_{2\uparrow}, \quad (22)$$

where \uparrow (\downarrow) represents the spin direction, and ρ_i represents the DOS for the spin channel of the layer i . Meservey *et al.* [12] further pointed out that the polarizations of electrons in the electrodes can be defined as:

$$P_1 = \frac{\rho_{1\uparrow} - \rho_{1\downarrow}}{\rho_{1\downarrow} + \rho_{1\uparrow}}, \quad (23)$$

$$P_2 = \frac{\rho_{2\uparrow} - \rho_{2\downarrow}}{\rho_{2\downarrow} + \rho_{2\uparrow}}. \quad (24)$$

The TMR can therefore be written as a function of the electron polarizations in both electrodes:

$$\text{TMR} = \frac{J_P - J_{AP}}{J_{AP}} = \frac{2P_1P_2}{1 - P_1P_2}. \quad (25)$$

Jullière's model explains the relation between the tunneling current and the DOS in the spin channels of electrodes, but does not consider the influences of many key MTJ physical parameters (e.g., the potential height and the asymmetry of the barrier) on the electrical behaviors of MTJs, thereby providing inaccurate modeling in practical applications [13].

3.1.2 Slonczewski's Model

Slonczewski improves Jullière's model by considering the effect of the angle of the magnetization orientations in both FM layers in an MTJ [14]. The free electron model is

applied to describe the behaviors of electrons. It also made assumptions that the MTJ is at 0 K without bias voltage and only electrons with a wave vector perpendicular to the barrier at the Fermi level contribute to the calculation of conduction. In particular, the conductance for one spin-transfer channel with a given parallel or antiparallel configuration can be expressed as:

$$G_{\sigma\beta} = \frac{e^2}{8\pi^2\hbar} \cdot \frac{\bar{\kappa}T_P}{d}, \quad (26)$$

where α and β are the notations for spin channels in both FM layers with four possible scenarios (i.e., $\uparrow\uparrow$ for spin-up conduction in parallel state, $\downarrow\downarrow$ for spin-down conduction in parallel state, and $\uparrow\downarrow$ and $\downarrow\uparrow$ for spin-up and spin-down conduction in antiparallel state, respectively), e is the electrical charge of an electron, \hbar is the planck constant, d is the thickness of the barrier layer, T_P is the conventional particle transmissivity, and $\bar{\kappa}$ is the mean wave vector of the evanescent wave in the barrier with the following definition:

$$\bar{\kappa} = \sqrt{\frac{2m_e}{\hbar^2} \Phi - k_{\parallel}^2}, \quad (27)$$

where m_e is the effective electron mass, Φ is the mean barrier potential height, k_{\parallel} is the component of the wave vector parallel to the tunnel junction layers and can be expressed as $\sqrt{2m_e E/\hbar^2}$, where E is the tunneling energy of electrons.

The conductance can be further expressed as a function of effective electron wave vectors of both electrodes in terms of κ_1 , κ_2 , k_1^σ , k_2^σ :

$$G_{\sigma\beta} = \frac{e^2 \bar{\kappa}}{8\pi\hbar d} e^{-2\bar{\kappa}d} \frac{\kappa_1 \kappa_2 k_1^\alpha k_2^\beta}{(\kappa_1^2 + k_1^{\alpha 2})(\kappa_2^2 + k_2^{\beta 2})}, \quad (28)$$

$$\kappa_1 = \sqrt{\frac{2m_e}{\hbar^2} \left(\bar{\Phi} + \frac{\Delta\Phi}{2} - k_{\parallel}^2 \right)}, \quad (29)$$

$$\kappa_2 = \sqrt{\frac{2m_e}{\hbar^2} \left(\bar{\Phi} - \frac{\Delta\Phi}{2} - k_{\parallel}^2 \right)}, \quad (30)$$

$$k_1^\sigma = \sqrt{\frac{2m_e}{\hbar^2} (E + \sigma\Delta)}, \quad (31)$$

$$k_2^\sigma = \sqrt{\frac{2m_e}{\hbar^2} (E + \sigma\Delta + eV)}, \quad (32)$$

where κ_i is the wave vector of the evanescent wave in the i th FM layer, $\Delta\Phi$ is the asymmetry of the barrier (i.e., the potential difference of the two electrodes), k_i^σ is the wave vector of a tunneling electron in the i th layer in the relative spin direction, σ equals to $+1$ (-1) in k_1 and k_2 corresponding to the relative spin orientation \uparrow (\downarrow) based on the magnetization, and Δ is one-half of the exchange splitting between the two spin bands of the FM electrodes [15].

The TMR definition of Slonczewski's analysis is of the same form as that proposed by Jullière, but with an improved term in the calculation of the spin polarization for the effective tunneling density of states:

$$P_{\text{eff}} = \left(\frac{k_{\uparrow} - k_{\downarrow}}{k_{\uparrow} + k_{\downarrow}} \right) \left(\frac{\bar{\kappa}^2 - k_{\uparrow}k_{\downarrow}}{\bar{\kappa}^2 + k_{\uparrow}k_{\downarrow}} \right). \quad (33)$$

Figure 3.1 illustrates the difference between the TMR as a function of the Fermi level polarization P in Jullière's and Slonczewski's models [5], [14]. The TMR generally increases with increasing polarization for each model. It is observed that Jullière's model does not describe the TMR well for barriers with different thicknesses, whereas Slonczewski's model provides a relatively more reasonable description of the free electron tunneling through a potential barrier. However, Slonczewski's model still cannot match with experimental results well since the effective polarization relates not only with the FM material, but also with the barrier potential height and the magnetization alignment with the other FM layer.

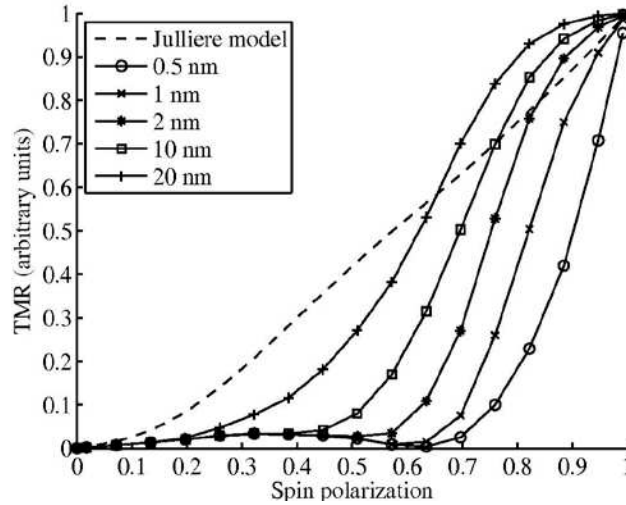


Figure 3.1 TMR variation with increasing Fermi level polarization as defined by Jullière's and Slonczewski's model with a barrier height of 1.7eV; the barrier thicknesses for the calculation with Slonczewski's model are 0.5 nm, 1 nm, 2 nm, 10 nm, and 20 nm.

In addition, Slonczewski pointed out the conductance of a tunnel junction varies with the angle θ between two magnetization orientations, which is given by:

$$G(\theta) = \bar{G}(1 - P_1 P_2 \cos\theta), \quad (34)$$

where \bar{G} is the mean conductance of the MTJ, and P_1 and P_2 represents the polarization of both electrodes, respectively.

Slonczewski's model presents a more accurate estimation over Jullière's model on the conductance, but it unfortunately ignores the effects of the applied voltage on the conductance, resulting in the constancy of conductance in response to the time-varying bias voltage. Also, the calculation of the angle θ in the above equation from the mean magnetizations of the two FM layers is not a trivial task and will be elaborated in section 3.3.

3.1.3 Simmon's and Brinkman's Model

Simmons derived an analytic equation for the tunneling effect through a potential barrier based on WKB approximation approach [16], in which a square barrier approximation is applied to an arbitrary barrier shape. The current density was calculated at low temperature so as to ignore the thermal current effect. This model was verified with experiment results in terms of the proportionality of current density to the applied voltage [17].

It was not until 1969 that Brinkman [18] established a parabolic conductance approximation model for a standard tunnel junction with a low-voltage range ($\leq 0.4V$)

and a relatively thicker (≥ 1 nm) barrier. The tunneling conductance of tunnel junctions with a trapezoidal barrier can be calculated by WKB approximation [18] given by:

$$\frac{G(V)}{G(0)} = 1 - \frac{A_0 \Delta \Phi}{16 \Phi^{\frac{3}{2}}} eV + \frac{9A_0^2}{128 \Phi} e^2 V^2, \quad (35)$$

where $G(0)$ is the conductance at zero bias, and A_0 is a constant relevant to the barrier thickness d :

$$A_0 = 4\sqrt{2m_e} \frac{d}{3\hbar}. \quad (36)$$

Although both models can demonstrate the general parabolic nature of the voltage-dependent conductance, Brinkman's model is still superior over Simmons' model in that Brinkman's model considers the asymmetry characteristic of the barrier potential height (i.e., the shift of the minimum conductance from zero bias) and is more preferable in the electrical tunneling modeling for voltage-dependent conductance calculation. However, Brinkman's model predicts that the conductance turns to be more independent of the bias voltage when the barrier thickness gets thicker, which is in conflict with experiments reported in the literature [64].

As reviewed above, each of these three models has its advantages and limitations, but none of them can be independently employed to reliably represent the electrical behaviors of the MTJ. A more comprehensive model is therefore critically needed and will be proposed in the following section for more accurate voltage-dependent conductance calculation.

3.2 Improved MTJ Electrical Tunneling Model

3.2.1 TMR Definition

The TMR definition in Jullière's model fails to predict the effects of the bias voltage on the performance of the MTJ [19], which can be analytically rectified with the addition of a fitting function:

$$\frac{TMR(V)}{TMR(0)} = \frac{V_h^2}{V_h^2 + V^2}, \quad (37)$$

where $TMR(0)$ is the TMR at zero bias, and V_h is the fitting voltage at which TMR is half of the peak value. Figure 3.2 shows an example of TMR-V curve in which the TMR varies with respect to a small bias (i.e., from $-1V$ to $1V$) for a symmetric MTJ at 0 K. The barrier is Al_2O_3 of 1 nm thick with a potential height of $1.7 eV$, and the electrodes are of the same material and geometry. The fitting parameter $V_h = \pm 0.82 V$ can be extracted from the fitting curve for either positive or negative bias voltage. The TMR at zero bias is approximately 4.7%. It should be noted that when the barrier is not symmetric, the fitting curve can be asymmetric at zero bias and the V_h for positive and negative bias will become different in the TMR fitting function. Such barrier asymmetry is mainly caused by the slight variations in the FM layer materials and the bias voltage. When the materials of the electrodes change, their coercivity will vary accordingly, leading to a tilt in the potential barrier; also when the MTJ is biased by an external voltage, the potential barrier will be tilted, forming a trapezoidal shape.

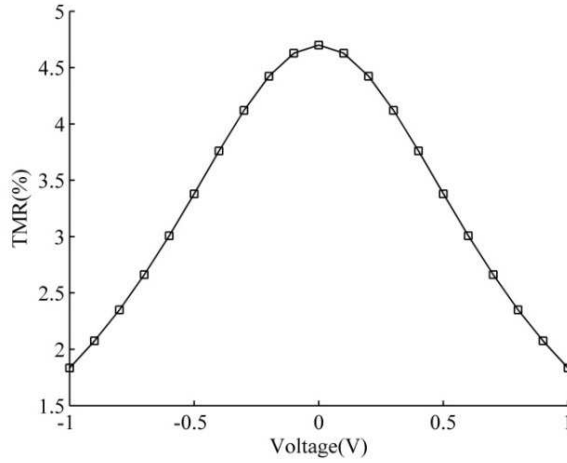


Figure 3.2 Rectified TMR versus bias voltage.

3.2.2 Modified Conductance Model

Brinkman's work intends to predict the behavior of the MTJ at a low bias (i.e., from -1V to 1V), and the conductance is determined as a function of the bias voltage and the initial conductance (i.e., the conductance at zero bias):

$$G(V) = G(0) \left[1 - \frac{A_0 \Delta \Phi}{16 \Phi^{\frac{3}{2}}} eV + \frac{9A_0^2}{128 \Phi} e^2 V^2 \right], \quad (38)$$

where the mean barrier height Φ and the barrier asymmetry $\Delta \phi$ are equal to $U + |V|/2$ for the MTJ with identical electrodes, and U is the barrier height at zero bias. If the FM electrodes of the MTJ are different metals or alloys, the effect of the coercivity difference should also be considered in the estimation of $\Delta \Phi$.

The angle-dependent conductance calculation (34) in Slonczewski's work can be used to determine the conductance at zero bias for any arbitrary configuration with an angle θ . However, the polarizations of the FM layers in this equation are derived from Jullière's

work in which the polarizations are independent of the bias voltage. It is therefore necessary to modify the conductance expression by integrating the TMR fitting function (37):

$$G(0, \theta) = \bar{G}(0) \left[1 + \frac{TMR(0)}{2 + 2 \left(\frac{V}{V_h} \right)^2 + TMR(0)} \cos \theta \right]. \quad (39)$$

The mean conductance at zero bias $\bar{G}(0)$ is relevant to the conductances in parallel and antiparallel configurations, G_P and G_{AP} . The $\bar{G}(0)$ for the identical electrodes in this work is only relevant to the mean potential height and the barrier thickness, and can be effectively integrated with the above model as a function of the conductances for different spin channels based on equations (4) to (6) and (28):

$$\begin{aligned} \bar{G}(0) &= \frac{G_{\uparrow\uparrow} + G_{\downarrow\downarrow} + G_{\uparrow\downarrow} + G_{\downarrow\uparrow}}{2} \\ &= \frac{e^2}{16\pi\hbar} \frac{\bar{\kappa}}{d} e^{-2\bar{\kappa}d} \left[\frac{\kappa_1 \kappa_2 k_1^\uparrow k_2^\uparrow}{(\kappa_1^2 + k_1^{\alpha 2})(\kappa_2^2 + k_2^{\uparrow 2})} + \frac{\kappa_1 \kappa_2 k_1^\downarrow k_2^\downarrow}{(\kappa_1^2 + k_1^{\downarrow 2})(\kappa_2^2 + k_2^{\downarrow 2})} \right. \\ &\quad \left. + \frac{\kappa_1 \kappa_2 k_1^\uparrow k_2^\downarrow}{(\kappa_1^2 + k_1^{\uparrow 2})(\kappa_2^2 + k_2^{\downarrow 2})} + \frac{\kappa_1 \kappa_2 k_1^\downarrow k_2^\uparrow}{(\kappa_1^2 + k_1^{\downarrow 2})(\kappa_2^2 + k_2^{\uparrow 2})} \right]. \end{aligned} \quad (40)$$

In this case, the resulting mean conductance will be not only a function of the barrier height and the barrier thickness, but also the asymmetry $\Delta\Phi$ of the barrier and the wave vector component k_{\parallel} .

Given the angle θ , the Slonczewski's equation (34) and the TMR fitting function (37) can be employed for calculating the conductance. Meanwhile Brinkman's approximation (35)

can be used to determine the mean conductance for MTJs operating under low voltages. After some mathematical manipulations with equations (34), (35) and (37), the conductance can be eventually expressed as a function of bias voltage V and the configuration of magnetization directions:

$$G(V, \theta) = \bar{G}(0) \left(1 - \frac{A_0 \Delta \Phi}{16 \Phi^2} eV + \frac{9A_0^2}{128 \Phi} e^2 V^2 \right) \left(1 + \frac{TMR(0)}{2 + 2 \left(\frac{V}{V_h} \right)^2 + TMR(0)} \cos \theta \right). \quad (41)$$

The resulting I-V curve is not a straight line through the origin, and this voltage-dependent conductance implies that the MTJ does not obey the Ohm's law. As such, the conductance can be defined as the derivative dI/dV , i.e., the differential conductance. The current across the MTJ would be the integration of the conductance with respect to the applied voltage:

$$I(V, \theta) = \int G(V, \theta) dV. \quad (42)$$

In practice, the conductance G would be the slope of the I-V curve and the present current can be iteratively calculated from the discrete voltages and the previous current:

$$I_i = G_i(V_i - V_{i-1}) + I_{i-1}, \quad (43)$$

where i is the step index of the applied voltage, the conductance and the current.

These improved modeling approaches for the conductance and current of the MTJ could provide a more accurate estimation on the MTJ electrical performance compared to

previous modeling approaches. It is worth mentioning that the calculation of the angle θ is not a trivial task, which will be elaborated in the following section.

3.3 Dynamic Magnetization in MTJ

The dynamic simulation proposed in this work is achieved by implementing the LLG equation in the finite element analysis, and the simulation results can facilitate the interpretation of the effective magnetic field, the magnetization angle for FM electrodes, and the micromagnetic behaviors.

3.3.1 The Calculation of Effective Field and Angle θ

The external magnetic field applied on an MTJ will affect the magnetizations of both FM layers. However, the effective field for one FM electrode is different from that for the other. The effective field is determined not only by the external magnetic field, but also by the demagnetizing field generated by the magnetization of the FM layer itself and the coupling field generated from the magnetization of the other FM layer. The coupling interaction between two FM layers is usually complex, especially when considering the pinhole coupling due to the pinhole defects in the barrier layer [20], the exchange coupling due to the spin polarization of FM layers [14], the Néel “orange-peel” coupling due to interface roughness [21], and the dipolar coupling originating from the stray fields at the edges [22]. The effective field calculation for a FM electrode is given as:

$$\vec{H}_{eff} = \vec{H} + \vec{H}_{demag} + J \cdot \vec{M}' + \vec{H}_{anis},$$

where \vec{H}_{demag} is the demagnetizing field, J is the coupling coefficient, \vec{M}' is the magnetization of the other FM layer, and \vec{H}_{ani} is the anisotropy field. Specially, the

demagnetizing field \vec{H}_{demag} can be expressed as an integral over the interior volume Ω of the body of the FM electrode [23]:

$$\vec{H}_{demag}(\mathbf{r}, T) = \frac{1}{4\pi} \int_{\Omega} d\mathbf{r}' \mathbb{D}(\mathbf{r} - \mathbf{r}') \cdot \vec{M}[H(\mathbf{r}', T), \mathbf{r}', T] \approx -\mathbb{N} \cdot \vec{M}, \quad (44)$$

where \mathbb{D} and \mathbb{N} denote the symmetric 3×3 demagnetizing tensor in different forms [24], [25], \mathbf{r} is the vector for the nodes inside and outside the body, \mathbf{r}' denotes the center of the node cells, and T is the temperature.

The coupling coefficient J is a function of the barrier thickness corresponding to the overall coupling interaction effect [26]:

$$J = J_0 \exp(-2\sqrt{2}\pi d / \lambda), \quad (45)$$

where J_0 is the constant coupling coefficient and λ is the characteristic distance, and these two parameters are usually determined from experimental results. It should be noted that the parameter λ will vary with respect to the thickness of the barrier layer [27].

The anisotropy field \vec{H}_{anis} is relevant to the anisotropy energy that derives from the interaction between the electronic field and the magnetic moments. Therefore the anisotropy field introduces preferential directions for the magnetization (i.e., easy axis or anisotropy axis) and is responsible for the motion of the magnetization vector around the easy axis. For the FM electrodes in this work, the anisotropy of the electrodes is considered to be uniaxial and the corresponding anisotropy energy density is given as:

$$E_{anis} = -K_1 \times (\vec{v}_{ea} \cdot \vec{m})^2 - K_2 \times (\vec{v}_{ea} \cdot \vec{m})^4, \quad (46)$$

where K_1 and K_2 are the second-order and fourth-order phenomenological anisotropy constants, respectively; \vec{v}_{ea} is the easy axis vector in the material object, and \vec{m} is the normalized magnetization of the layer.

By ignoring K_2 for calculation simplicity, the anisotropy field can be given as:

$$\vec{H}_{anis} = \frac{2K_1}{\mu_0 M_{sat}^2} (\vec{v}_{ea} \cdot \vec{m}) \cdot \vec{v}_{ea}. \quad (47)$$

The angle θ between the two magnetizations is relevant to the orientations of both FM layers and can then be conveniently calculated as:

$$\cos\theta = \frac{\vec{M}_1 \cdot \vec{M}_2}{\|\vec{M}_1\| \cdot \|\vec{M}_2\|}, \quad (48)$$

where \vec{M}_1 and \vec{M}_2 are the averaged three-dimensional magnetization vectors of each FM layer.

3.3.2 Dynamic Magnetization Simulation

The LLG equation describes the time evolution of magnetization in a ferromagnetic material [28]:

$$\frac{\partial \vec{M}}{\partial t} = -\gamma \mu_0 \vec{M} \times \vec{H}_{eff} + \frac{\alpha}{M_{sat}} \vec{M} \times \frac{\partial \vec{M}}{\partial t} - \frac{v}{M_{sat}^2} \vec{M} \times (\vec{M} \times \hat{j} \cdot \nabla \vec{M}) - \frac{\xi v}{M_{sat}} \vec{M} \times \hat{j} \cdot \nabla \vec{M}, \quad (49)$$

where \vec{M} is the magnetization of the material, \vec{H}_{eff} is the effective magnetic field, μ_0 is the vacuum permeability, α is the damping factor, M_{sat} is the saturation magnetization, $\gamma = g \cdot \mu_B / \hbar$ is the gyromagnetic factor where μ_B is the Bohr magneton constant and g is

the Landé factor that is approximately 2 for most magnetic materials [29], $\hat{j} \cdot \nabla$ is the derivative along the direction of the current, ξ is the degree of non-adiabaticity, and v is given as:

$$v = \frac{Pj\mu_B}{eM_{sat}(1 + \xi^2)}, \quad (50)$$

The first term $\mu_0 \vec{M} \times \vec{H}$ on the right-hand side of the equation (49) represents the torque derived from Zeeman energy [29] and the spin-field interaction. It tends to align \vec{M} to the direction of \vec{H}_{eff} , resulting in a precessional motion of \vec{M} around \vec{H}_{eff} . The second term $\frac{\alpha}{M_{sat}} \vec{M} \times \frac{\partial \vec{M}}{\partial t}$ models the energy loss of the magnetization precession around the applied field by a Gilbert damping constant α , which is relevant to the electrode material [30]. The third term $\frac{v}{M_{sat}^2} \vec{M} \times (\vec{M} \times \hat{j} \cdot \nabla \vec{M})$ and the fourth term $\frac{\xi v}{M_{sat}} \vec{M} \times \hat{j} \cdot \nabla \vec{M}$ intend to include the spin-transfer torque (STT) effect and the non-adiabaticity circumstance [31].

The STT effect is relevant to the current flowing through the MTJ [32] and was first reported by Slonczewski [14]. When a current flows through an MTJ, it becomes polarized and the transverse component of the spin in the flowing electrons can be transferred to the conduction electrons, therefore exerting a torque on the local moments of the electrodes and influencing the precessional behavior of the magnetization. Figure 3.3 illustrates the schematic of the magnetization precession in the LLG equation. Without considering the damping factor, the magnetization motion will be periodic and move around the magnetic field axis (i.e., the circle in Figure 3.3).

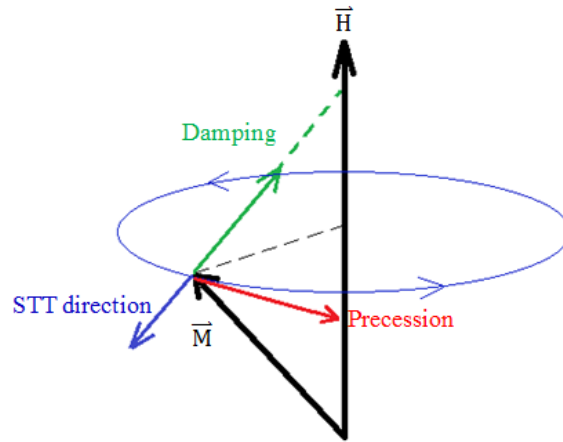


Figure 3.3 Directions of precession, damping and spin-transfer torque vectors in LLG model.

An analog simulation for the dynamic magnetizations of an MTJ is carried out in this work in the python programming with a set of material entities, field libraries and function scripts, aiming at providing accurate time evolutions of magnetizations under a magnetic field.

More specially, a material entity contains a series of independent functions for the declaration and definition of the FM material properties; a field library sets up the magnetic field, the magnetization field, or the energy density in the FM electrodes; the comprehensive electrical tunneling model and the LLG equation are numerically implemented in the function scripts for the dynamic magnetization calculations. In addition, all variables in the material entities and the field libraries are set with the international system of units (SI units), which is invoked from an independent unit definition function.

In this study, the geometry of the MTJ is firstly defined as a mesh by employing the finite element analysis method *imprimis*, allowing the numerical analysis for each node in the mesh. The MTJs are defined as identical cuboid FM electrodes ($100 \times 100 \times 10 \text{ nm}^3$) sandwiching a barrier layer with the same area, as illustrated in Figure 3.4. Each node in the mesh has 3 degrees of freedom (i.e., x, y and z components) for the magnetizations and the magnetic fields of the FM layers. The boundary conditions are the continuity of the spin current density of each spin transport channel $J_{\alpha\beta}$ and $\partial \vec{m} / \partial z = 0$ at the interfaces of the two FM layers and the barrier layer, where z is the direction perpendicular to the MTJ multilayer planes.

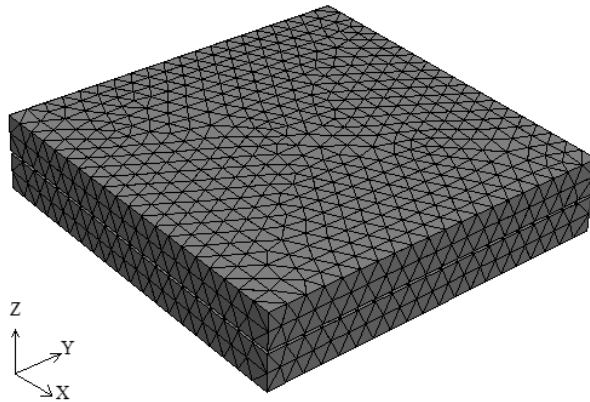


Figure 3.4 The generated tetrahedral mesh of an MTJ with 1 nm barrier layer by Netgen [33].

A material entity contains the declaration and initialization of the parameters for one FM layer, including a list of strings for the material name, the saturation magnetization, the anisotropy coefficients, the exchange coupling energy density, and the parameters for the LLG equation, respectively. These parameters can be conveniently called or modified in other calculating functions.

In total, three kinds of fields are defined in the system to describe the magnetic behaviors of the FM layers: the magnetizations of the electrodes, the magnetic fields (including the external field, the exchange coupling field, the anisotropy field, the demagnetizing field, and the total effective field) for each electrode in the MTJ mesh, and the energy densities (scalar field) corresponding to the magnetic fields. These fields are expressed as the arrays of three-dimensional vectors for each node in the geometry mesh and are numerically calculated based on their definitions.

To achieve the time-evolution of the magnetization vectors in the three-dimensional space, the LLG equation is implemented in the simulation. For a given external magnetic field vector and given magnetizations of the FM layers, the LLG equation calculates the changes of the magnetizations for each node in the electrodes within a nano-scale period until the magnetizations reach their equilibrium states (i.e., $\partial\vec{M}/\partial t \approx 0$). To this end, the magnetization relaxation process and the dynamic magnetizations of the electrodes can be approximated.

By calculating the relaxed magnetizations with an array of magnetic fields in a period, the hysteresis loop of the magnetization for the free layer can be achieved. A few points that are critical for the calculation of the magnetizations of each layer are elaborated below:

- The magnetizations of the nodes in the pinned layer are set as constant vectors in the function, such that they remain unchanged during the simulation. In practice, this pinning effect can be realized by a layer of antiferromagnetic material close to the pinned layer through Ruderman-Kittel-Kasuya-Yosida (RKKY) interactions [34].
- The effects to the determination of the effective field caused by the demagnetizing field, the exchange coupling from the other FM layer, and the anisotropy field are implemented. The effective field thus will vary from one electrode to the other and change as the external magnetic field changes.
- The STT effect is considered with a current density function based on the comprehensive electrical tunneling model, and the interaction between the polarized current and the magnetizations are calculated iteratively.

3.4 Simulation Result

The analytical analysis and simulation have been carried out using both MATLAB and python programming. The target device in this work is the MTJ with the composition of $\text{Co}_{40}\text{Fe}_{40}\text{B}_{20}$ (10 nm)/ Al_2O_3 (d)/ $\text{Co}_{40}\text{Fe}_{40}\text{B}_{20}$ (10 nm) MTJ biased by an external voltage source and subjected to a static magnetic field.

3.4.1 Electrical Characteristic

Based on the improved electrical tunneling model discussed in Chapter 3, the voltage-dependent characteristics of the MTJ can be obtained. The essential parameters that are used for the analysis are listed in Table 1. It should be noted that the electron tunneling energy and the barrier height can be measured through experiments and the parameters listed in the table are only for simulation purpose.

Table 1 Parameters for tunneling electrical model

Symbol	Quantity	Value
E	electron tunneling energy	0.7eV
U	barrier height	1.7eV
Φ	mean barrier height	$U+0.5V$
V_h^+	V_h for positive voltage	0.8V
V_h^-	V_h for negative voltage	-0.8V
TMR_0	TMR at zero bias	4.7%

Figure 3.5 shows the variations in MTJ conductance and current with respect to the low bias voltage (ranging from $-1V$ to $1V$, respectively) for both parallel (i.e., $\theta = 0$) and antiparallel (i.e., $\theta = \pi$) configurations. The simulation results indicate: 1) the conductance for an MTJ in antiparallel configuration is lower than that in parallel configuration, which is in accordance with the TMR mechanism of the MTJ; 2) the conductance does not reach minimum point at zero bias due to the asymmetry of the barrier height; and 3) the difference in terms of current for these two configurations is not obvious when the applied voltage is low.

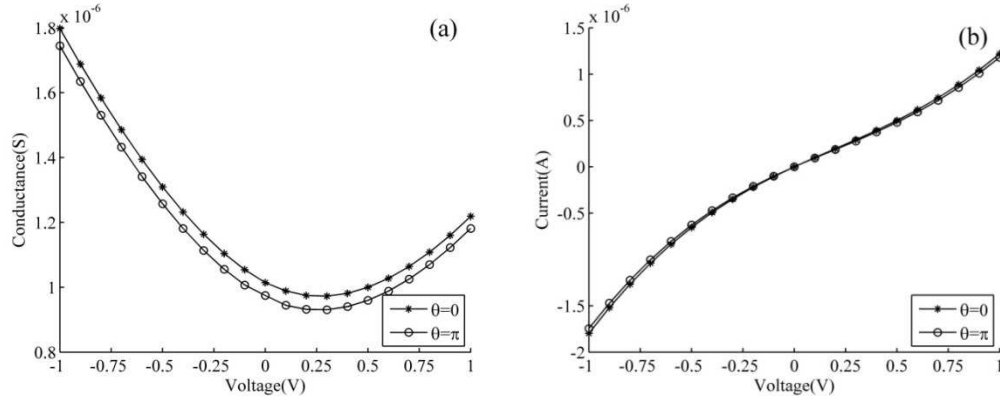


Figure 3.5 The simulated electrical characteristics of the MTJ in both parallel and antiparallel configurations: (a) the G-V curve; (b) the I-V curve.

Figure 3.6 shows the conductance calculated from both the Brinkman's model and the improved electrical tunneling model. The MTJ is in the parallel configuration, with a barrier thickness of 1 nm and a barrier potential height of 1.7 eV. A conductance increment can be observed in the improved tunneling model, which derives from the conductance in each spin tunneling channels.

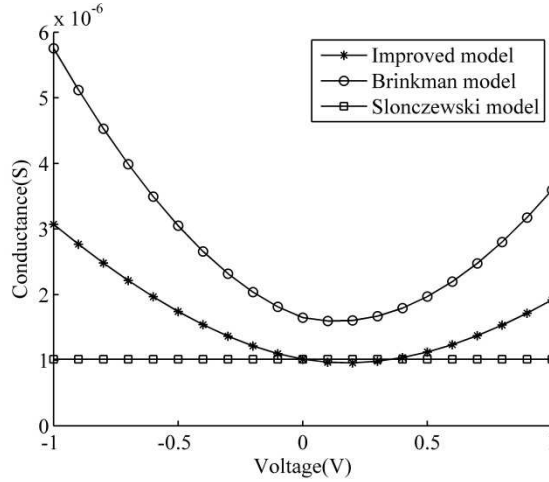


Figure 3.6 Conductance comparison calculated from the Slonczewski’s model, Brinkman’s model and the improved electrical tunneling model with a barrier thickness of 1 nm and a barrier potential height of 1.7 eV.

The thickness of the barrier layer also affects the MTJ performance significantly. Figure 3.6 shows the effects of the barrier thickness towards the current and conductance with a bias voltage of 1V. As the thickness of the barrier layer increases, the current decreases dramatically. It can also be observed that the current-voltage and conductance-voltage dependence will reverse when the barrier thickness reaches 1.6 nm (Figure 3.6 (b)), and the MTJ current and conductance scales are much lower than those with barrier thicknesses under 1.0 nm.

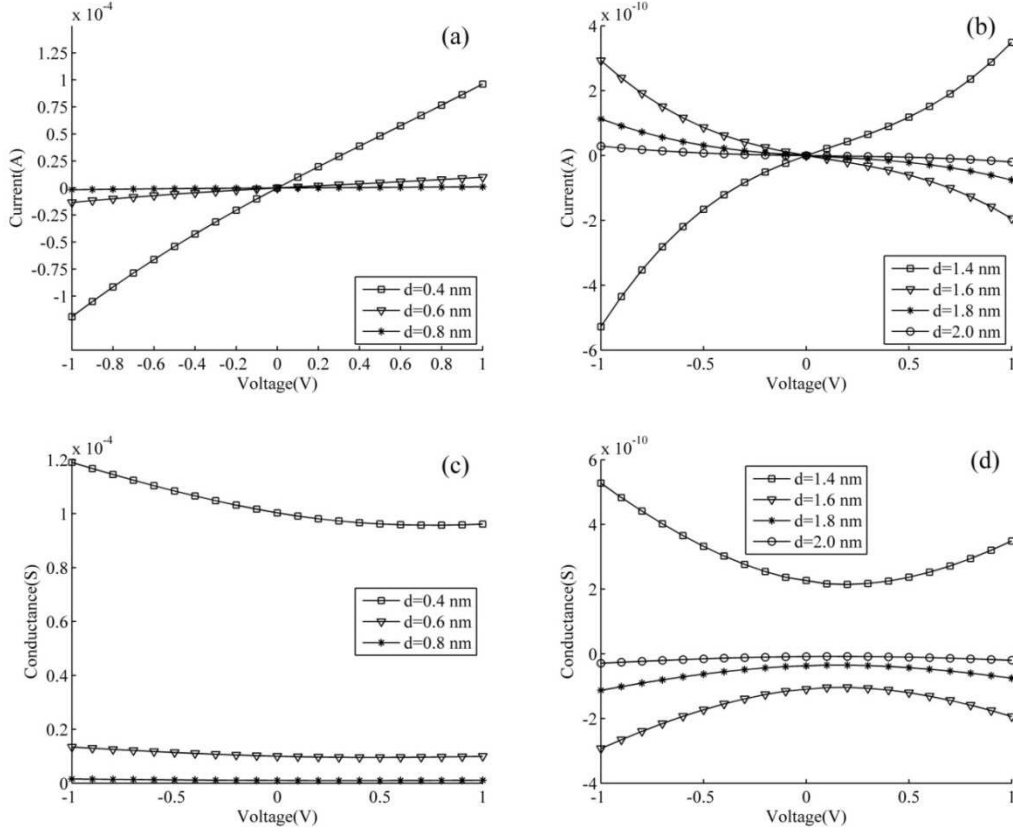


Figure 3.7 The voltage-dependent current and conductance comparisons of the MTJ for different barrier thicknesses: (a) Current for thicknesses under 1.0 nm; (b) Current reversion phenomenon for large barrier thicknesses; (c) Conductance for thicknesses under 1 nm; and (d) Conductance reversion correspondingly for larger barrier thicknesses.

3.4.2 Dynamic Simulation

In this work, the magnetization is computed based on the LLG equation with an adiabatic condition (i.e., $\xi = 0$) to simplify the calculation. Figure 3.7 shows the LLG simulation for a $100 \times 100 \times 10$ nm³ FM cuboid with the 10 nm edge orienting along z direction. The easy axis and the initial magnetization are both set in the x direction. A polarized current is applied through the cuboid in z direction while an external magnetic field is set in the y direction. Figure 3.7(a) illustrates the time evolution of the average

magnetization in three-dimension space until an equilibrium state (i.e., $\partial\vec{M}/\partial t \approx 0$) is reached, and Figure 3.7(b) shows the normalized average magnetization versus the relaxation time in three directions. It is observed that the magnetization tends to align with the applied field during its relaxation process, and the precession trajectory forms a damped circle.

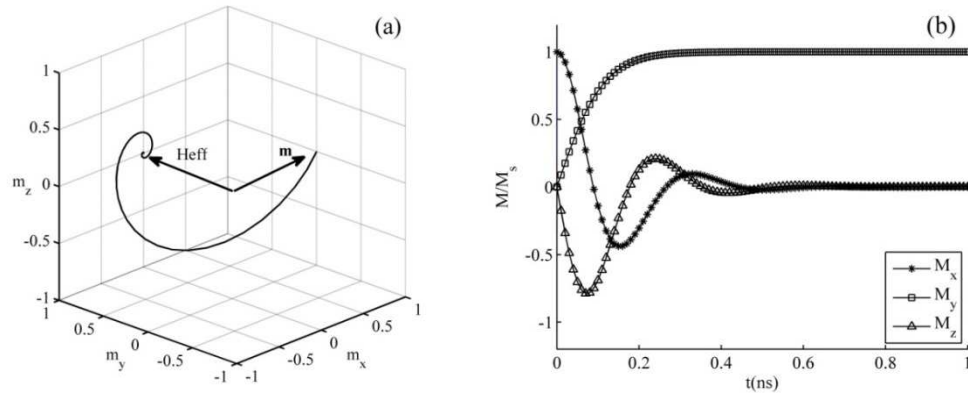


Figure 3.8 The trajectory of the magnetization of a cuboid based on LLG model: (a) Three-dimensional evolution of the magnetization vector; (b) Transient change of M_x , M_y and M_z within 1 ns.

The dynamic magnetization behavior of a $\text{Co}_{40}\text{Fe}_{40}\text{B}_{20}$ (10 nm)/ Al_2O_3 (d)/ $\text{Co}_{40}\text{Fe}_{40}\text{B}_{20}$ (10 nm) MTJ has also been simulated. Table 2 lists the parameters of the $\text{Co}_{40}\text{Fe}_{40}\text{B}_{20}$ FM electrodes used in simulation. The easy axis of the two FM layers are set perpendicular to each other and are set in the x-y plane (i.e., x-direction for the pinned layer and y-direction for the free layer, which makes the magnetization of the free layer mildly hysteretic and approximately linear with the applied field. This is appropriate for field sensor applications [35]. The initial normalized magnetization vectors of both layers are set along the easy axis of the pinned layer. It should be noted that the initial normalized

magnetization vector is slightly distorted by adding a tiny component in the y direction since the x direction is an unstable equilibrium direction for the magnetization anisotropy of the free layer. In addition, the uniaxial anisotropy only considers the second-order phenomenological anisotropy constant K_1 , and the parameters J_0 and λ are chosen as 0.05 and 10 nm for the simulation.

Table 2 Material properties in the dynamic magnetization simulation

Symbol	Quantity	Value
M_{sat}^a	saturation magnetization	623.59 A/m
\vec{m}	initial normalized magnetization vector	[1, 0.017, 0]
E_{exch}^b	exchange coupling	4.5×10^{-12} J/m
K_1^c	1 st -order uniaxial anisotropy constant	2.5×10^4 J/m ³
γ	gyromagnetic ratio	2.211×10^5 m/A s
α	LLG damping factor	0.5
J_0	constant coupling	0.05
λ	characteristic distance	10 nm
P	current polarization	0.5

^aFrom Landolt-Börnstein Database [36] for $\text{Co}_{40}\text{Fe}_{40}\text{B}_{20}$ at room temperature.
^{b,c}Evaluated from experimental results by S. V. Komogortsev *et al.* [37].

The simulation results are illustrated in the following Figure 3.8 and Figure 3.9. The y-axes shown in Figure 3.8 are the normalized average magnetization vectors for the free FM layer in the MTJ mesh after the relaxation process. The magnetization along z-direction M_z is very small compared to the magnetizations along x and y directions and is therefore ignored. The barrier thickness is set as 1 nm. As shown in Figure 3.8(a), the magnetization along the direction of applied field forms a hysteresis loop and the

magnetization within the applied field from -50 kA/m to 50 kA/m is nearly linear, which is desired for sensor application.

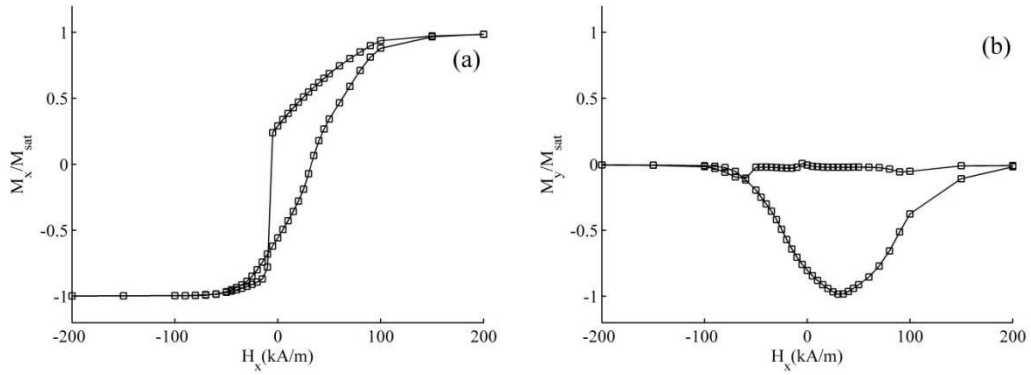


Figure 3.9 The dynamic behavior of the free layer magnetization for an MTJ with 1 nm barrier: (a) $M_x - H$ curve; (b) $M_y - H$ curve.

The angle between the magnetizations of the two FM layers can be calculated from the averaged magnetization vectors and has been illustrated in Figure 3.9(a). It is noted that there is a switching phenomenon around zero magnetic field when the magnetic field decreases, whereas the magnetization increases smoothly when the magnetic field increases to reach the initial intensity. By integrating the improved electrical tunneling model iteratively in the dynamic magnetization simulation, the current-field dependence of the MTJ with a bias voltage of 0.5 V and a barrier thickness of 1 nm is obtained, given in Figure 3.9(b). These simulation results are consistent, in terms of the minimum resistance, the maximum resistance, and the linearity, with experimental results reported in the previous works. Figure 3.11 shows the comparison between the experimental result reproduced from the literature [38] and the simulation result based on the parameters in the experiment.

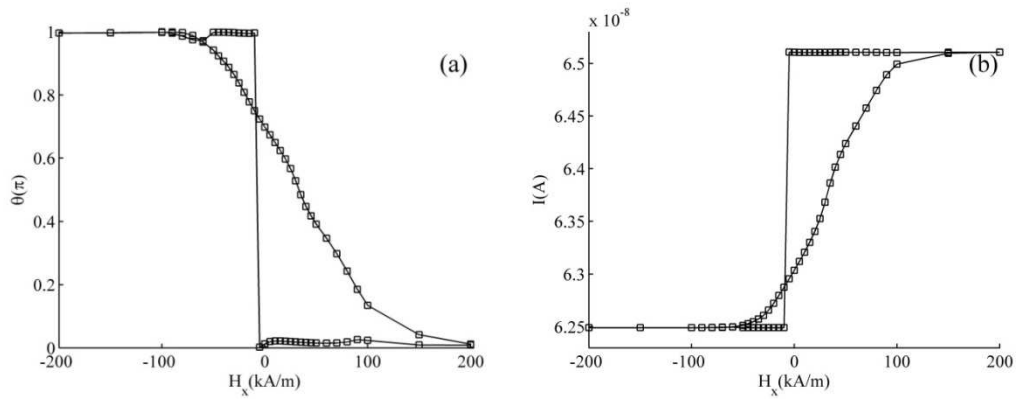


Figure 3.10 The magnetic field dependence of the angle θ between the magnetizations of two FM layers and the current across the MTJ: (a) $\theta - H_x$ curve; (b) $I - H_x$ curve.

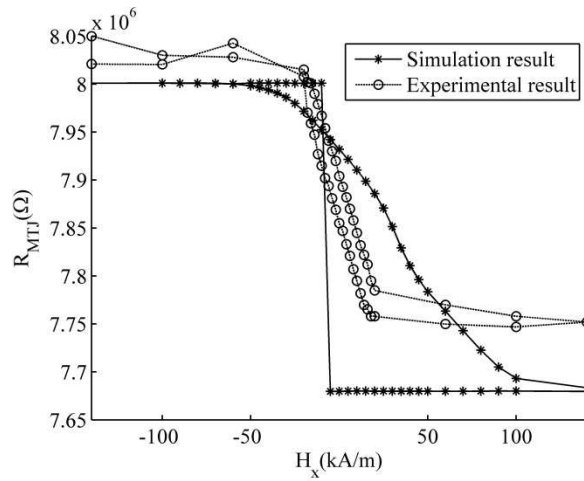


Figure 3.11 Resistance comparison of an MTJ from the experimental results reproduced from the literature [39] and the simulation result with the parameters from the experiment.

In summary, the proposed approach integrating an improved electrical tunneling model and the dynamic magnetization simulation can well describe the behavior of MTJs with the low bias voltage, the static magnetic field, and the uniaxial anisotropic ferromagnetic electrodes under an adiabatic condition. The simulation results matches well with experimental results reported in the previous works.

Chapter 4. Magnetic Sensor Design Based on MTJ

In this chapter, the structure design and the fabrication process of the magnetic sensors based on the MTJ effect will be presented as a preparation for future experimental works. The structure and the material selections for the MTJ sensor designs will be determined in section 4.1, followed by the function descriptions for each layer in section 4.2. The details of the sensor design will be further discussed in terms of the MTJ naming conventions, the design of electrodes and the photoresist masks with the alignment marks. The fabrication process and the relevant equipment will be presented in section 4.8.

4.1 MTJ Sensor Design

A MTJ sensor structure in this work contains the following layers (thicknesses in nm): substrate/ Ta (100)/ $\text{Co}_{50}\text{Fe}_{50}$ (2)/ NiMn (15)/ $\text{Co}_{50}\text{Fe}_{50}$ (2)/ Ta (1)/ $\text{Co}_{40}\text{Fe}_{40}\text{B}_{20}$ (3)/ Al_2O_3 or MgO (1) / $\text{Co}_{40}\text{Fe}_{40}\text{B}_{20}$ (10)/ Ta (100)/ Cu (100) (Figure 4.1). This is more complicated than the typical three-layer structure (i.e., the pinned layer / insulator / free layer structure) as the extra layers between the substrate and the junction are added to improve the MTJ performance. Specially, the MTJ structure designed in this work is composed of a substrate, a buffer layer, a seed layer, an AFM layer, a synthetic antiferromagnetic (SAFM) pinned layer, an insulating layer, a free layer, and finally the conductive capping layer, which is schematically shown in Figure 4.1.

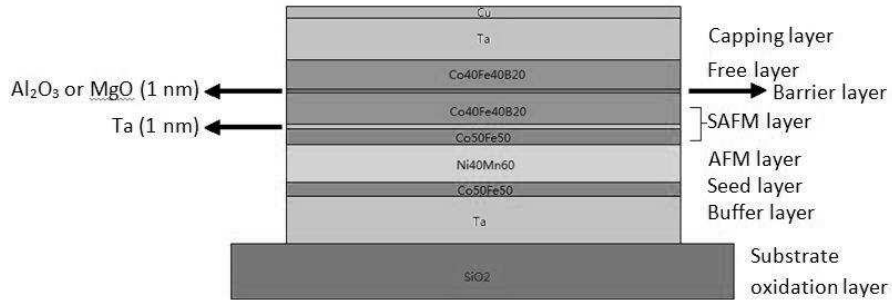


Figure 4.1 The schematic layout of the MTJ structure.

4.2 The Function Descriptions of Each Layer

4.2.1 Substrate

The substrates for the MTJs in this work are standard silicon wafers (2" in diameter, 275 μm in thickness), provided by the Carleton University's Microfabrication Facility (CUMFF). Silicon wafers are extremely flat, exhibiting high thermal conductivity, good stability and adhesion properties, and are thus chosen as the substrates. Wafers are thermally oxidized to form a layer of 1 μm ($\pm 10\%$) SiO₂, oriented in (100) direction prior to the deposition of the MTJ stack. This process prevents potential short circuiting on the silicon wafer surface. The thickness of the oxidation layer is measured by an ellipsometer to ensure the surface smoothness.

4.2.2 Buffer Layer

The buffer layer is deposited so as to achieve a better MR for MTJs since it acts as the bottom lead and helps improve the texture of the AFM films above it [40]. The material for the buffer layer can be tantalum (Ta), platinum (Pt) or ruthenium (Ru) [41] and the smoothness of this layer is critical to ensure the flatness of subsequent layers. The chosen

material for the buffer layer in this work is Ta with a thickness of 100 nm. Ta has an electrical resistivity of 131 nΩ·m, which is relatively low and is capable of minimizing the overall resistance of the MTJ stack.

4.2.3 Seed Layer

A 2 nm thick Co₅₀Fe₅₀ layer is deposited as a seed layer adjacent to the buffer layer. The purpose of this layer is to reduce the lattice mismatch of the buffer layer and the following AFM pinning layer. An alternative material for this layer is permalloy (e.g., Ni₂₁Fe₇₉) [42].

4.2.4 Antiferromagnetic Layer

The material chosen for the AFM layer is NiMn (40/60 wt%, 15 nm), which acts as an exchange bias field source to antiferromagnetically pin the magnetization of the FM layer above it (i.e., the pinned layer) [43] as well as enable the growth of the subsequent layers. Alternative materials for this layer are limited to some Mn-based metallic alloys (e.g., FeMn, IrMn, NiMn, PtMn, PdMn etc.) or some insulating oxides (e.g., NiO, α – Fe₃O₄, etc.) [44]. Table 3 lists the exchange bias properties for the spin-valves with the AFM layers, among which PtMn, IrMn and NiMn exhibit good performances in terms of the exchange bias strength H_{exch} .

Typically IrMn (22/78 at%) is the most common material used for the AFM layer in MTJs, but NiMn is instead chosen in this work for cost consideration. The blocking temperature (T_b) of NiMn based MTJs is 400°C, higher than the T_b 225°C of IrMn based

MTJs, and the remnant blocking temperature distribution of NiMn is better than that of IrMn [45]. It is therefore suggested that NiMn based MTJs have far superior thermal durability and pinning stability at high temperatures than IrMn based MTJs.

Table 3 Exchange bias properties of spin-valve structures with different AF biasing layers [13]

AFM layer material	H_{exch} (Oe)	J_{exch} (erg/cm ²)	Bulk T_N (°C)
FeMn	250	0.11	210
IrMn	680	0.18	420
PtMn	690	0.18	500-700
NiMn	880	0.30	800
CrPdMn	620	-	380

4.2.5 Pinned Layer

A single pinned FM layer in an MTJ may encounter some problems such as the demagnetization when exposed in a strong external magnetic field, or the variation of the exchange bias between pinned layer and the AFM layer due to thermal variation of the magnetic properties. To gain an improved performance through the exchange bias effect between the pinned CoFeB layer and the AFM NiMn layer, a tri-layer structure (referred to as SAFM layers) can be applied. Figure 4.1 shows that instead of a single FM pinned layer, a tri-layer structure, Co₅₀Fe₅₀(2) / Ta(1) / Co₄₀Fe₄₀B₂₀(3) (thicknesses in nm) take place adjacent to the AFM layer. The two magnetic layers, Co₅₀Fe₅₀ and Co₄₀Fe₄₀B₂₀, are coupled by a short range RKKY interaction, which provides a strong exchange bias [46]. This design can minimize stray field effects that may cause asymmetry of the magnetic response of the free layer [47], increase the total TMR by its strong coupling, and facilitate the annealing process at a high temperature [48].

4.2.6 Barrier Layer

The insulating barrier layer is the most critical layer in an MTJ as it is required to be ultra-thin, surface smooth and pin-hole free. The material for this layer is usually insulating oxidation of metals such as Al_2O_3 and MgO . In microfabrications, it is hard to directly deposit a flat and smooth barrier layer with oxidation substances. An alternative method is to sputter the elemental metal (i.e., Al or Mg), and then oxidize the metal to form the desired oxidation thickness. It is also necessary to calibrate the process accurately so as to avoid any excess or deficit of the oxidation layer so as to prevent pin-holes and other defects.

In MgO MTJs, MgO barrier needs to form a crystalline structure along (001) direction. The CoFeB layer is reported to be essentially amorphous but partially crystallized after the annealing process [49]. Wang *et al.* reported that an improved crystallinity of the MgO (001) layer leads to a high TMR ratio at high annealing temperatures [55][56].

4.2.7 Free layer

An amorphous 3 nm $\text{Co}_{40}\text{Fe}_{40}\text{B}_{20}$ layer is deposited as the free FM layer. The FM layer can be partially crystallized during the annealing process to match the barrier orientation, which helps form (001) orientation barrier for MgO based MTJs and result in the “symmetry filtering effect” [50]. This effect at the barrier-electrode interface leads to a high TMR effect in MTJs with the MgO barrier, but does not exist in those with the amorphous Al_2O_3 barrier.

4.2.8 Capping Layer

The capping layer is 100 nm Ta, followed by 100 nm Cu. It is reported that the materials of the capping layer and the barrier layer can affect the MR ratio of MgO MTJ due to their influence on the crystallization process of the CoFeB free layer in the annealing process [49], [51], resulting in MR change. Copper is chosen as the final capping layer above Ta to act as the electrode and to prevent the oxidation of the structures beneath it.

4.3 MTJ Sensor Structure

The thickness of the barrier layer and the area of the MTJs are two key parameters for the MTJ sensor design. Therefore the footprints of the MTJ sensors are chosen exponentially from $1 \mu\text{m} \times 1 \mu\text{m}$ to $16 \mu\text{m} \times 16 \mu\text{m}$ squared on a wafer with the same barrier thickness. Deposition and oxidation methods can be modified to achieve different barrier thicknesses.

Since no experimental methods are ideal, the MTJ stack cannot be guaranteed to have extreme smooth interfaces and a pin-hole free characteristic of the barrier layer. This can be attributed to many factors such as the non-uniform deposition of materials over the wafer, contamination by the external environment, as well as potential oxidation during the fabrication processes. In order to achieve functional MTJs, 400 independent MTJs are designed to be patterned on one wafer. Each MTJ lies in the center of a cell with an area of $1.5 \text{ mm} \times 1.5 \text{ mm}$. Groups of ten MTJs, with tunneling areas varying from $1 \mu\text{m} \times$

1 μm to 16 $\mu\text{m} \times 16 \mu\text{m}$, are considered to be one block with an arrangement of 2 rows and 5 columns, allowing a 20 \times 20 grid of MTJ cells in total on the wafer.

Electrical contacts for external circuits should also be integrated in the MTJ sensor design. Electrodes should be located on both sides of the MTJ stack, allowing electrical currents to flow through the MTJ. One of the electrodes is on the surface of the MTJ with a contact pad (i.e., the top electrode), while the other one is buried between the substrate and the MTJ, which is then stretched to the MTJ surface as the other contact pad (i.e., the bottom electrode). A layer of Al_2O_3 will be deposited onto the wafer in order to prevent short circuit between the top and bottom contact pads. For each side of the electrodes, there are two contacting areas, which are large enough (50 $\mu\text{m} \times 50 \mu\text{m}$) for welding lines, and can prevent accidental physical damages caused by temperature or stress changes in the MTJs during the welding process. Figure 4.3 shows the design of the two electrodes. It should be noted that central column of the top electrode is 20 μm longer than that of the bottom electrode so as to separate them when the bottom electrodes stretch to the MTJ surface. The widths of these two central columns are both 20 μm , which is larger than the maximum length (16 μm) of the MTJ sensing unit, ensuring that the whole MTJ sensing unit is completely sandwiched by the two electrodes.

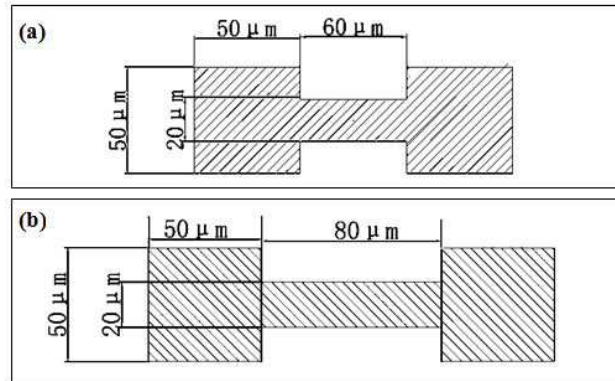


Figure 4.2 The electrode designs for the MTJs: (a)Bottom electrode design; (b)Top electrode design.

4.4 MTJ Naming Conventions

It is necessary to designate names for MTJ sensors on the wafers, allowing them to be identified during the subsequent measurements. MTJs in the cells of a wafer are assigned with unique identification numbers, which are composed of three parts: the batch ID, the thickness ID and the device ID. Only the last device ID will be etched onto the wafer in order to distinguish the MTJ. The batch ID numbers are based on the date of the initial MTJ film deposition; the thickness ID is based on the thickness of the MTJ barriers in nanometer; each individual MTJ device on the wafer is patterned with a unique device ID number, etched on the wafer by the photoresist masks during the photolithography. This unique ID number, which consists of several letters and numbers, reveals the block position and the size of each MTJ device on the wafer. Conditions for each MTJ are entered into a database with records on the fabricating environments and the product results.

For example, one particular MTJ might have the ID number: B23C4, as is shown in Figure 4.2. B23 means Block 23, and C4 indicates the cell position as well as the MTJ area.

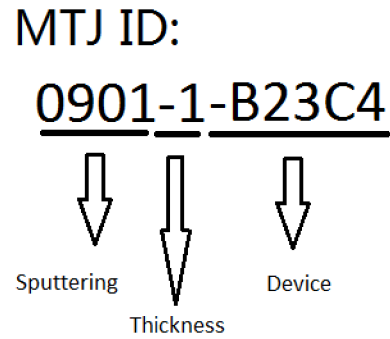


Figure 4.3 An example of the nomenclature of MTJ sensors.

4.5 Photoresist Masks

To fabricate the desired MTJ sensing unit, photoresist masks are needed for patterning and separating MTJs on the wafer in a process known as photolithography. Four photoresist masks, Mask 1 to Mask 4, are designed as shown in Figure 4.4.

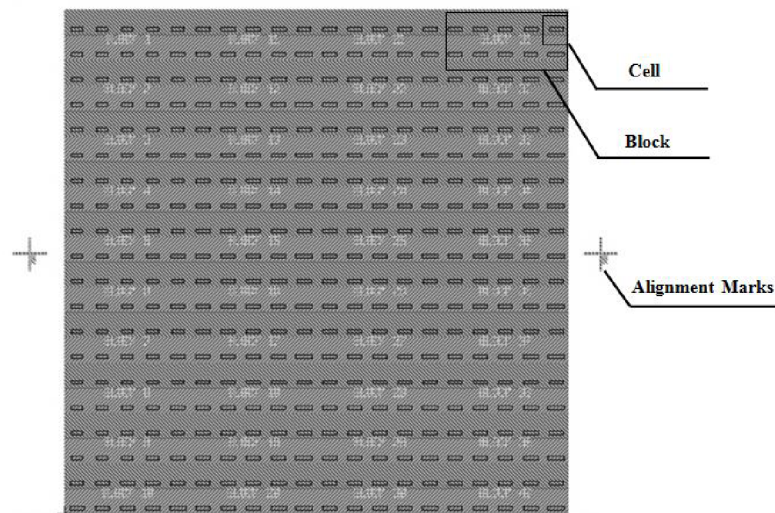


Figure 4.4 Masks aligned together for photolithography.

The materials described above are first deposited in sequence on the wafer. In the photolithography process, a layer of a photoresist material will be deposited onto the surface of the wafer prior to the use of each mask. When a photoresist mask is applied in the process, the photoresist material will be etched except the part within the shaded area on the mask (Figure 4.5-Figure 4.8). The deposited materials on the wafer will then be etched in the subsequent etching process with the remnant photoresist material as the patterning mask. Mask 1 defines the shape of the bottom electrode with two kinds of electrodes: one with a specific area described in section 4.5 (the top part in Figure 4.5 (a)), and the other one without any etching, leaving the entire buffer layer for the bottom electrode (the bottom part in Figure 4.5 (a)). Mask 2 defines the different MTJ tunneling area in each sensor cell (Figure 4.6). After the separation of the two electrodes by depositing an insulating layer of Al_2O_3 , Mask 3 generates the exposure area of the bottom electrodes and the tunneling area in the insulating material (Figure 4.7). Finally Mask 4 is applied after the deposition of copper, defining the top electrodes. All the numbering marks are created on the surface of the MTJ sensor cells by Mask 4 for the identification purpose (Figure 4.8).



Figure 4.5 Mask 1: (a) Example of one block in Mask 1; (b) Zoomed in details of one cell with the bottom electrode shape in Mask 1.

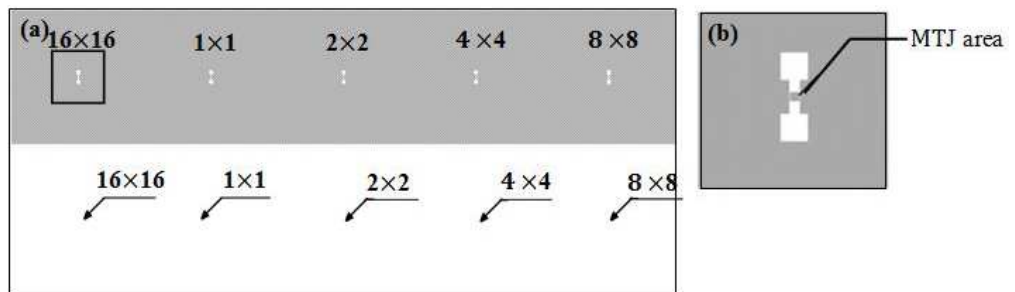


Figure 4.6 Mask 2: (a) Example of one block in Mask 2; (b) Zoomed in details of one cell with the MTJ area of $16\mu\text{m} \times 16\mu\text{m}$ in Mask 2.

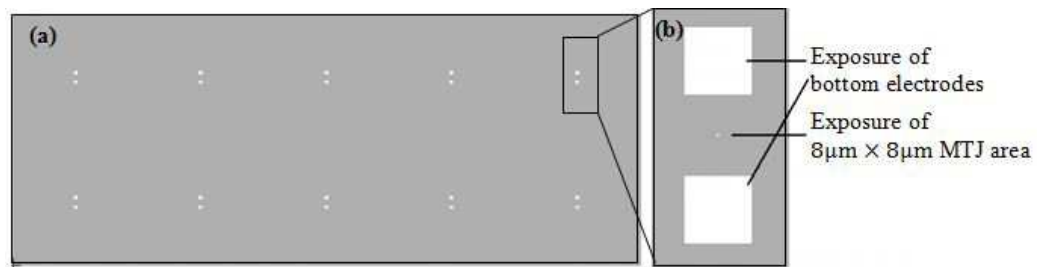


Figure 4.7 Mask 3: (a) Example of one block in Mask 3; (b) Zoomed in details of one cell with the exposure shapes for the bottom electrodes and the MTJ in Mask 3.

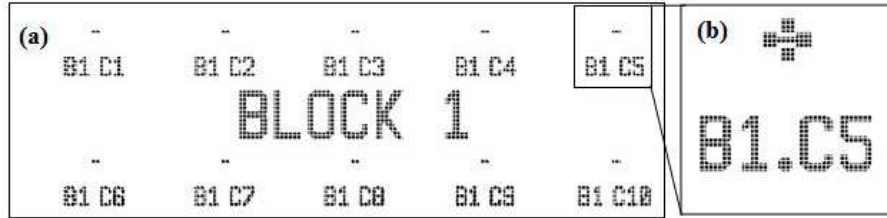


Figure 4.8 Mask 4: (a) Example of one block in Mask 4; (b) Zoomed in details of one cell with the shape of the top and bottom electrodes as well as the numbering marks in Mask 4.

4.6 Alignment Marks

In order to make functional MTJs, the patterns over different lithography steps for one MTJ structure must be aligned at the same location. This can be achieved by adding alignment marks on the photoresist masks. The first pattern transferred to a wafer includes a set of alignment marks on Mask 1, which exhibit high precision features and are considered as the references for positioning subsequent masks (Figure 4.9(a)). The two shades on Mask 2 and Mask 3 prevent the deposition of Al_2O_3 and copper onto the reference alignment mark, which ensures the accuracy of alignment. The jagged edges of the aligning cross shape are for resolution detection of the masks. The alignment marks are also numbered for identification (Figure 4.9(b-e)).

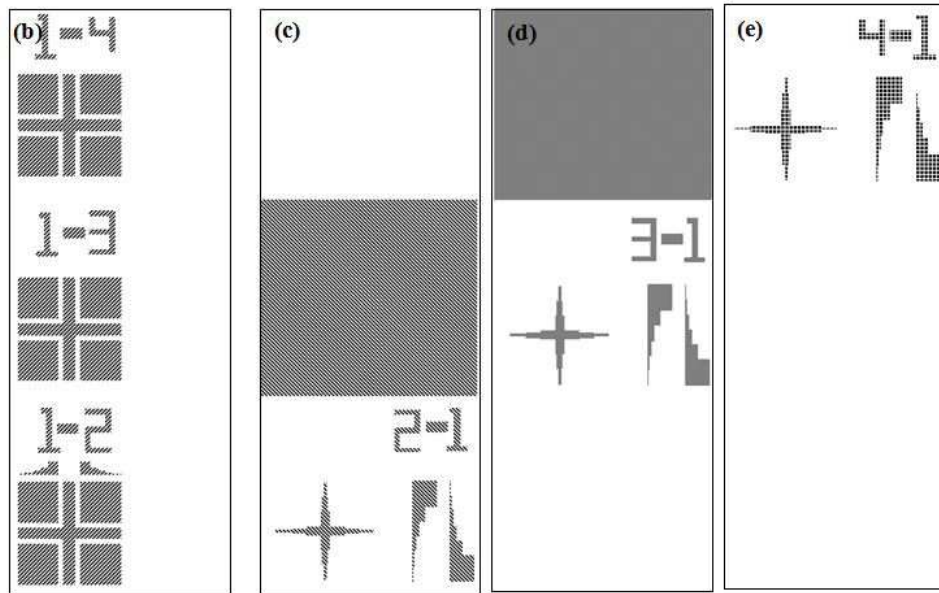
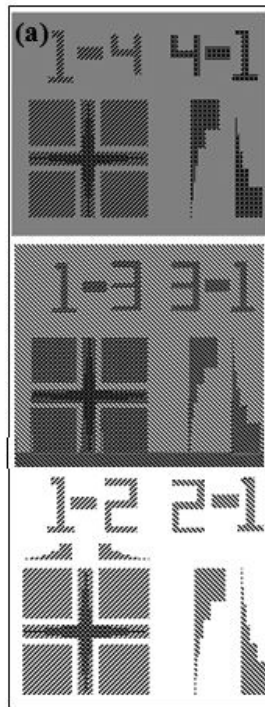


Figure 4.9 Alignment marks for four layers: (a) All 4 alignment marks align together; (b-e) Alignment marks 1 to 4 are shown separately with the shades and the numbers.

4.7 Fabrication Process

4.7.1 Equipment for Fabrication

High quality MTJ sensor development relies on a set of well-calibrated and reliable precision equipment. The equipment in the CUMFF is capable of manufacturing the required MEMS components through a series of microfabricating processes such as the selection of substrate, the deposition of target materials, the pattern transformation through etching and other necessary processes.

4.7.1.1 Substrate Preparation

Substrate preparation prior to the deposition process is required for producing clean and unscratched surfaces. SiO₂ wafers can be cleaned by the standard RCA cleaning process prior to the high temperature processes (e.g. annealing, diffusion, chemical vapor deposition (CVD), *etc.*). This procedure has been found very effective in producing extremely clean substrate wafers and has been taken as the standard cleaning procedure in many microfabrications. The cleaning processes are given below:

- i) Removal of the organic contaminations (Organic Clean),
- ii) Removal of the thin oxide layer (Oxide Strip),
- iii) Removal of the ionic contamination (Ionic Clean).

An oxidation layer needs to be formed on the surface of the wafer, which can be achieved by a high-temperature thermal oxidation process in a furnace, with the temperature rising up to 1100°C. An eight-stack Bruce Model BDF-8 furnace bank is available in CUMFF

for oxidation, annealing, pre-deposition and drive-in steps on wafers up to 100 mm in diameter. The furnace usually takes around 2 hours to generate the desired 1 μ m thick SiO₂ layer on the surface of a 2” silicon wafer over a wet oxidation process. The temperature, the pressure and the gas composition conditions of the furnace can be controlled, and the profiles of these parameters can be recorded for a later use [52].

4.7.1.2 Sputtering Deposition System

Sputtering deposition is a physical vapor deposition (PVD) process in which atoms are ejected from a solid host target at temperatures much lower than the vaporization temperature of the solid within a high vacuum environment. The work is done by numerous collisions between the target and the ionized and accelerated inert gaseous atoms such as Ar, resulting in a vapor traveling through the vacuum. Part of the ejected vapor reaches and condenses on the substrate, contributing to the desired film growth. By controlling the sputtering time and the average sputtering rates for different materials, the desired thicknesses of the sputtered layers can be obtained.

Direct current (DC) magnetron sputtering deposition will be used to generate the MTJ stack and the insulating and contacting layers. Films will be deposited in the designed sequence on the wafers without any lithography or photoresist masks in a four-stack Bruce model BDF-4 furnace bank (Figure 4.10) with cantilever loading. The control strategy for the temperature and gas flow is similar to that for the oxidation/diffusion furnaces. The layers of the materials will be deposited onto the wafer by DC sputtering from the bottom to the top. Three sputtering targets can be loaded into the equipment at a

time. During the deposition, the environmental conditions of the sputtering process will be recorded as well for future calibration purpose.



Figure 4.10 BDF-4 furnace in CUMFF [52].

4.7.1.3 Photoresist Mask Preparation and Photolithography System

The photoresist masks for photolithography have been prepared in the Micro & Nanofabrication Facility (NanoFab) at the University of Alberta. The masks were generated in a .tdb file format using the software L-Edit v11, which is the standard CAD tool supported and used by the NanoFab. The masks were then produced by a Pattern Generator (Heidelberg DWL-200) (Figure 4.11(a)). Lithography were carried out by a

Karl-Suss MA6 mask aligner (Figure 4.11 (b)), which can accept substrates ranging from small fragments to 100 mm diameter wafers.

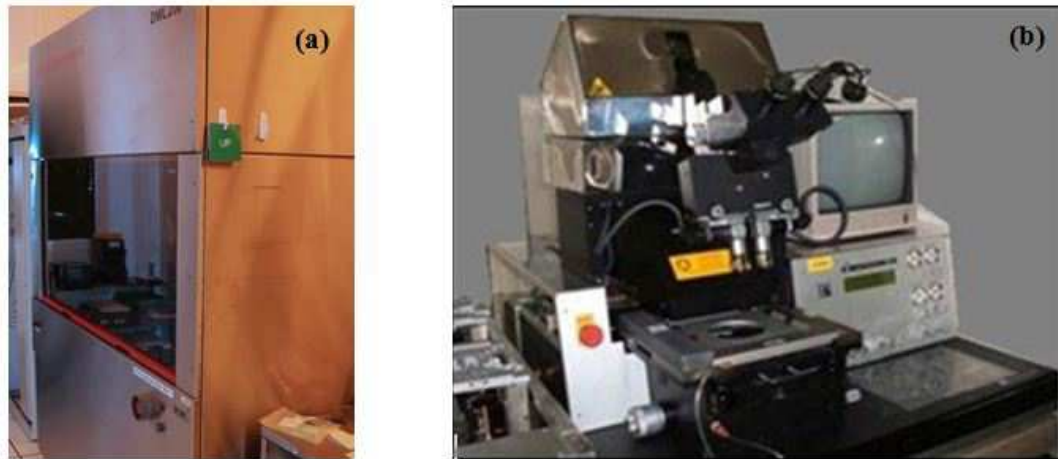


Figure 4.11 Facilities for photo masks and photolithography [52]: (a) Heidelberg DWL- 200 mask generator; (b) Karl-Suss MA-6 Aligner.

Figure 4.12 - Figure 4.15 show both sides of the sealed photoresist masks on which the structure patterning area, the numbering letters, and the alignment marks are observable. Specifically, the shaded rectangular areas (i.e., the unetched areas) above and below the MTJ cell array will be used for testing the interlayer characteristics of the MTJ stack.

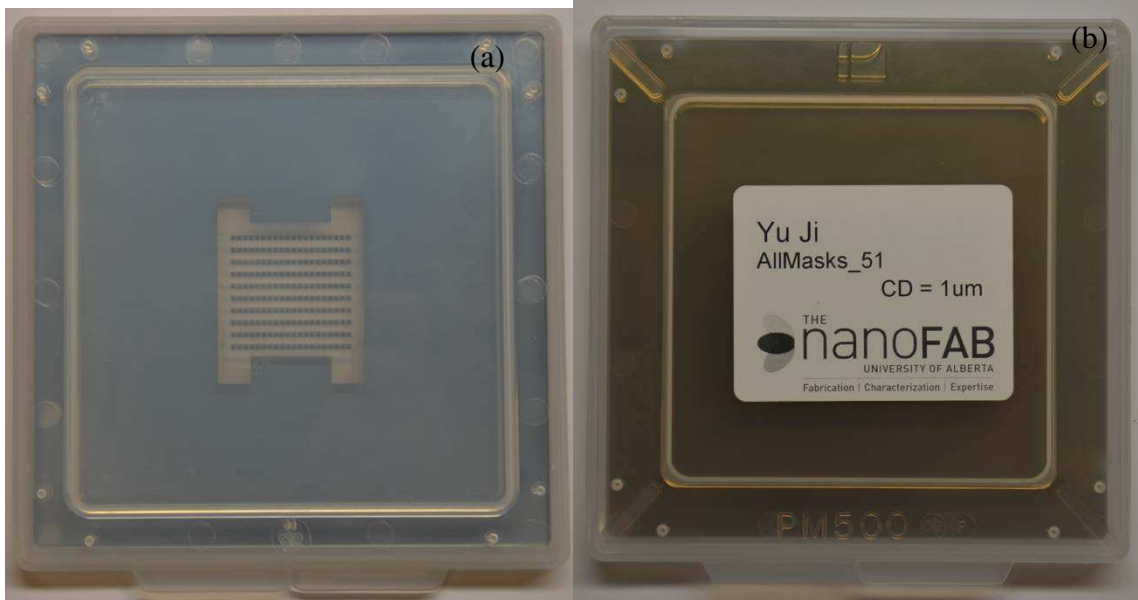


Figure 4.12 Fabricated photoresist mask 1: (a) The top side showing the mask patterns; (b) The bottom side showing the mask label.



Figure 4.13 Fabricated photoresist mask 2: (a) The top side showing the mask patterns; (b) The bottom side showing the mask label.

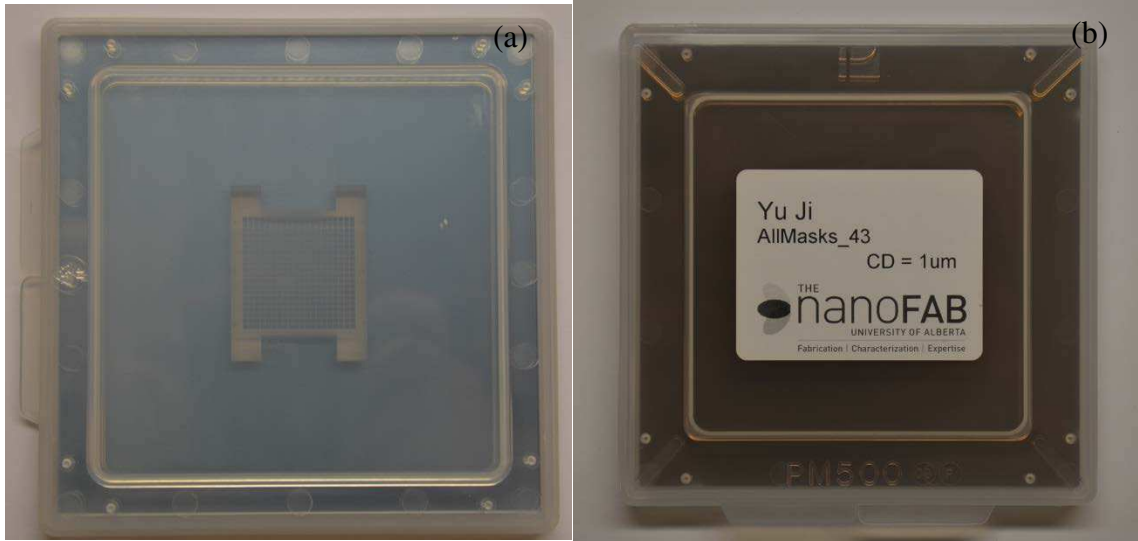


Figure 4.14 Fabricated photoresist mask 3: (a) The top side showing the mask patterns; (b) The bottom side showing the mask label.



Figure 4.15 Fabricated photoresist mask 4: (a) The top side showing the mask patterns; (b) The bottom side showing the mask label.

4.7.1.4 Etching System

After the patterns of each mask are transferred to the photoresist layer on the sample surface, the reactive-ion etching (RIE) process is applied to transfer the formed shape to the corresponding layer using a dry etching system such as the PlasmaTherm SLR-772/ ECR etcher (Figure 4.16). The plasma excitation power and the average ion bombardment energy at the substrate can be independently controlled. The maximum wafer diameter allowed in the system is 150 mm, and the uniform etching zone is 100 mm in diameter, which is large enough for the 2" (~51 mm) wafers in this project. The whole system is pumped with an Alcatel 5900 CP turbopump [52].

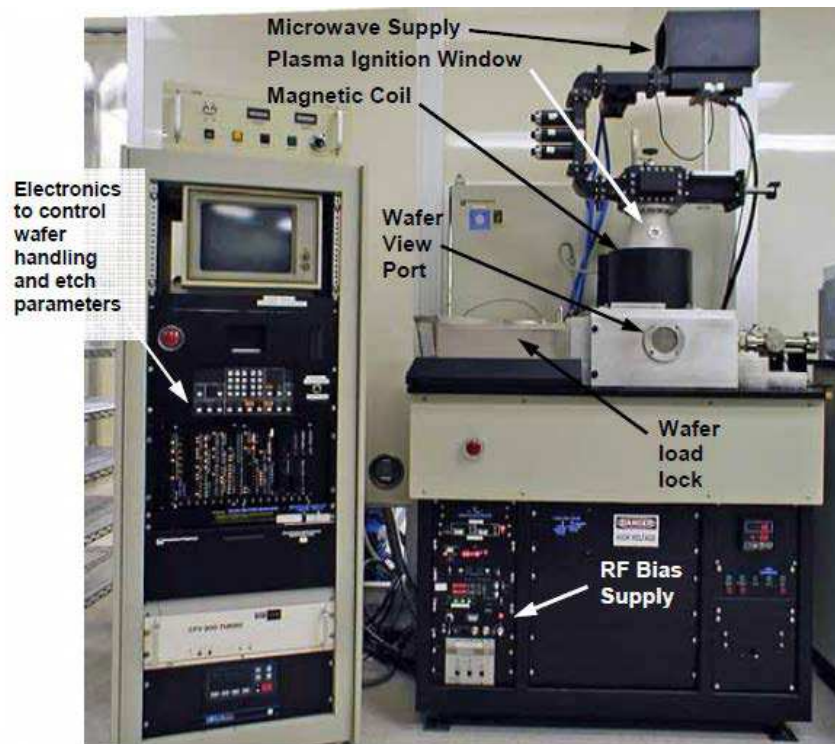


Figure 4.16 PlasmaTherm SLR-772 ECR RIE [53].

4.7.1.5 Magnetization and Annealing

The thermal annealing process is an essential step for the development of both Al_2O_3 based MTJs and MgO based MTJs. This step needs to be performed after the deposition and oxidation of the barrier layer and under high vacuum environments with protective gas (e.g., Ar) so as to prevent any oxidation reaction on the samples.

To generate a functional tunnel junction, the CoFeB FM layer beneath the barrier layer needs to be pinned based on the exchange bias effect with the AFM layer during the annealing process. This is a very challenging task but can be achieved using the Micro Magnetics SpinTherm 1000 Magnetic Thermal Annealing System located in the Nanofabrication Laboratory at Carnegie Mellon University (Figure 4.17). When the MTJs are heated up to a temperature between the Neel temperature of the AFM layer (T_N) and the Curie temperature of the FM layer (T_C , where $T_C > T_N$), the directional anisotropy of the magnetic domains in the FM materials can be destroyed. The layers are then cooled to the room temperature under an applied magnetic field in plane, which defines the new directional anisotropy field in the materials. This process aligns the magnetization of the FM layer to that of the adjacent AFM layer, forcing its “easy axis” to be in line with the desired direction [35]. The exchange bias can therefore be created and the magnetization direction of the CoFeB layer can be fixed.



Figure 4.17 The Micro Magnetics SpinTherm 1000 Magnetic Thermal Annealing System [66].

4.7.1.6 Process Monitoring

An Applied Materials Technology AME 550 Ellipsometer is available in the CUMFF for measuring the silicon oxidation thickness of the wafer as well as the whole MTJ stack deposition. Software has been prepared by the CUMFF to allow the application of ellipsometer to multi-layer MTJ stacks. Accuracy is approximately +/- 1 nm for thin oxide layers [52].

4.7.1.7 Atomic Layer Deposition System

The atomic layer deposition (ALD) system located at the National Institute of Standards and Technology (NIST) will be employed for depositing the ultra-thin barrier layers to ensure its uniform and pin-free properties (Figure 4.18). The ALD process has several

advantages over other techniques for depositing thin films and is especially advantageous when the high film quality is required. This technique is also quite effective in coating substrates with ultra-high aspect ratio or substrates that would be difficult to be coated with other thin film techniques such as sputtering.

The ALD process allows accurate thickness control to the atomic level and deposits the film material of approximately one atomic thickness in each run, which possesses the following characteristics:

- Pinhole-free films over very large areas,
- Excellent repeatability,
- Wide process windows (no sensitivity to temperature or precursor dose variations),
- Available on amorphous or crystalline, depending on substrate and temperature,
- Digital control of sandwiches, heterostructures, nanolaminates, mixed oxides, graded index layers, and doping,
- Insensitivity to dust contamination (and ability to grow underneath dust),
- Standard recipes for oxides, nitrides, metals, and semiconductors.



Figure 4.18 The Atomic Layer Deposition System: Oxford FlexALRPT [67].

4.7.1.8 Dicing and Packaging

Following the depositions and etching steps, the wafers should be diced into blocks for testing. A Micro Automation 1006 diamond saw, a Tempres diamond scribe, a Unitek 8-146-06 thermocompression wirebonder and a West Bond 7400 A ultrasonic wire bonder are available in the CUMFF for the packaging of small quantities of MTJ sensor samples [52].

4.7.2 Fabrication Process

The fabrication procedure of the MTJs with the structure described in section 4.2 is schematically shown in Figure 4.19, in which the lower figure at each fabrication step is the cross-section of the A-B plane (Figure 4.19(a)). The MTJ materials are first deposited

onto the wafer in sequence and then etched to form the bottom electrodes and tunneling structure based on photolithography using the photoresist masks (i.e., Mask 1 and Mask 2). After depositing an insulating layer, the bottom electrodes and top electrodes are separated to avoid short circuiting. The top electrodes, the alignment marks, and the indices for each MTJ are generated by using Mask 3 and Mask 4 afterwards. A schematic structure of a typical MTJ sensor is shown in Figure 4.20.

The fabrication steps mentioned above are listed below:

- i) Produce a 1 μm SiO_2 layer on the silicon wafer,
- ii) Deposit the MTJ multilayers by sputtering in sequence,
- iii) Chemical etching in photolithography by Mask 1, defining the bottom electrode,
- iv) Chemical etching in photolithography by Mask 2, defining the MTJ layers,
- v) Deposit the SiO_2 layer to isolate the top and bottom electrodes,
- vi) Chemical etching in photolithography by Mask 3 to expose the bottom electrode,
- vii) Chemical etching in photolithography by Mask 4 followed by Ta layer deposition to define the top contact pad and bottom contact pad,
- viii) Anneal the sample with a uniform magnetic field in plane under high vacuum environment.

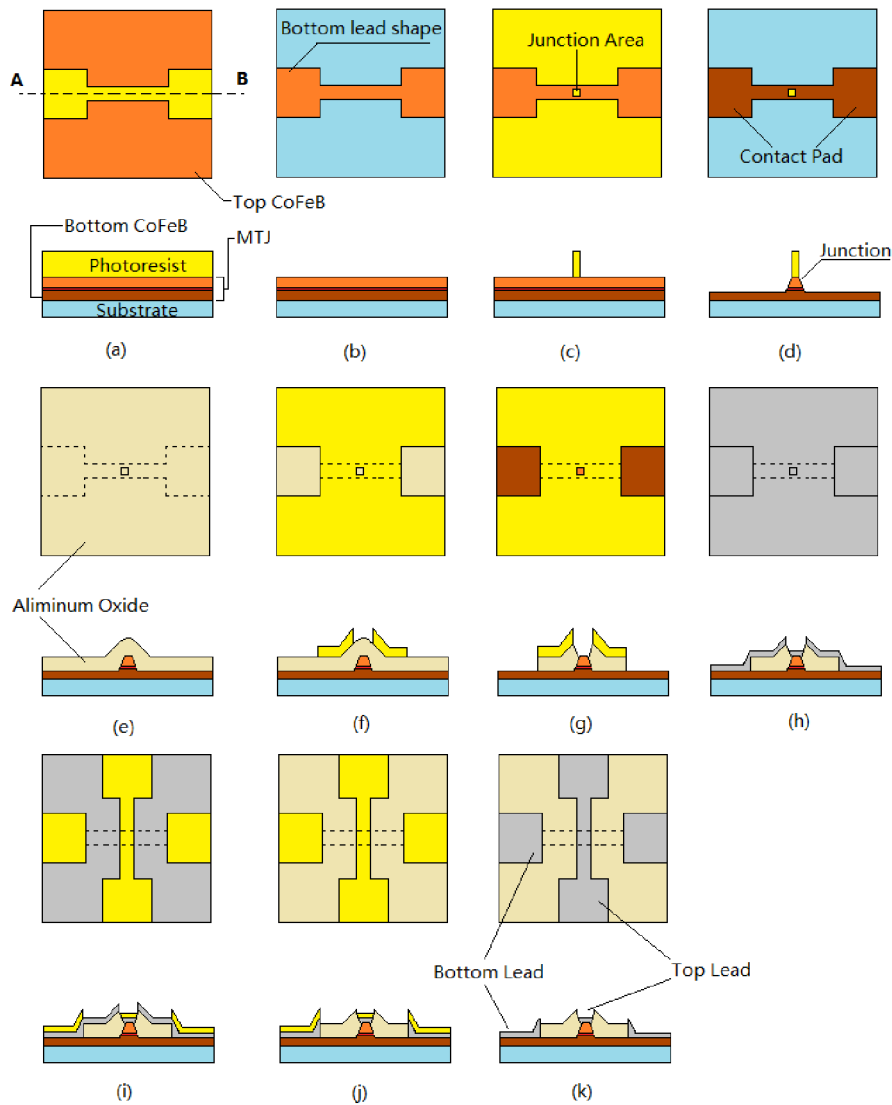


Figure 4.19 Schematic diagram of the MTJ fabrication processes: (a) As-deposited film (simplified with the MTJ stack) after sputtering; (b) The first patterning and first etching step for bottom electrode; (c- d) After the second patterning and first etching step, the tunnel junction area is defined; (e) The insulator layer is deposited around the tunnel junction for separating the bottom and top electrodes; (f- k) After the exposure of the bottom electrode, the Ta bottom and top contact pads are defined.

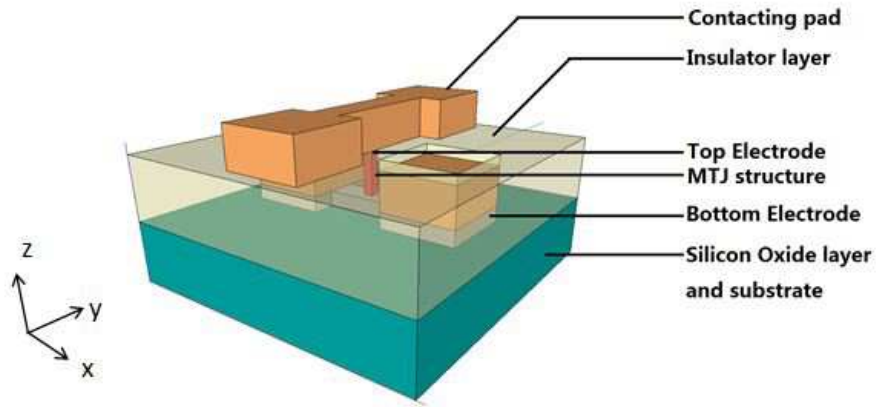


Figure 4.20 Three dimensional structure of a MTJ sensor after fabrication.

4.7.3 Fabrication Plan

As mentioned earlier, 400 MTJ sensing units in total with different tunneling areas will be generated and experimentally tested in future research work. Table 4 summarizes these MTJ wafers with different configuration.

Table 4 Wafers of MTJs with different configurations

Conditions Wafer Number	SAFM structure	Barrier material	Barrier Thickness(nm)
NO.1	No	Al ₂ O ₃	2.0
NO.2	No	Al ₂ O ₃	1.8
NO.3	No	Al ₂ O ₃	1.6
NO.4	No	Al ₂ O ₃	1.4
NO.5	No	Al ₂ O ₃	1.2
NO.6	No	Al ₂ O ₃	1.0
NO.7	Yes	Al ₂ O ₃	2.0
NO.8	Yes	Al ₂ O ₃	1.8
NO.9	Yes	Al ₂ O ₃	1.6
NO.10	Yes	Al ₂ O ₃	1.4
NO.11	Yes	Al ₂ O ₃	1.2
NO.12	Yes	Al ₂ O ₃	1.0
NO.13	Yes	MgO	2.0
NO.14	Yes	MgO	1.8
NO.15	Yes	MgO	1.6
NO.16	Yes	MgO	1.4
NO.17	Yes	MgO	1.2
NO.18	Yes	MgO	1.0

To this end, the sputtering targets required for the fabrication of MTJ sensors have been purchased from Kurt J. Lesker Company with a purity of 99.99% (4N) for the copper target and 99.95% (3N5) for other target material. The structures of the MTJ sensors have been designed and the corresponding photoresist masks have been produced in the NanoFab at the University of Alberta. The fabrication processes as well as the required equipment have been studied, and the fabrication plan for the designed MTJ sensors has been given.

Chapter 5. Conclusion and Future Works

5.1 Conclusions

Although several modeling approaches have been reported in the literature for magnetic tunnel junctions (MTJs), none of them can be employed to reliably and accurately predict the electrical properties of MTJs. Accordingly in this work, a novel MTJ modeling approach has been presented to address this challenge. The proposed approach integrates an improved electrical tunneling model and the dynamic magnetization simulation. The suggested MTJ model characterizes MTJs with the low bias voltage, the static magnetic field, and the uniaxial anisotropic ferromagnetic electrodes under an adiabatic condition. The electrical aspects arising from both the external conditions (e.g., bias voltage, voltage-dependent conductance, etc.) and the internal properties (e.g., tunnel magnetoresistance (TMR), barrier asymmetry, etc.) of the MTJ are all considered to describe the MTJ behaviors in a more comprehensive way. The improved electrical model is implemented in the dynamic magnetization simulation based on the finite element analysis, which leads to more accurate simulation results in the case that spin-transfer torques take place. The simulation results are in line, in terms of the minimum resistance, the maximum resistance, and the linearity, with experimental results reported in the previous works. In the meantime, a new type of magnetic sensors based on magnetic tunnel junction technology has been designed, and will be fabricated and tested in the future research work. A study will be conducted to compare the results from both experiments and simulation with a purpose to further improve the design of the MTJ sensor.

5.2 Future Works

Future research should be conducted in the following subjects:

- 1) The proposed model will be further improved to include the effect of the non-adiabatic condition as well as the thermal and stress distribution on the magnetization variations of the simulated MTJ.
- 2) A more complex MTJ will be established in the simulation to consider the synthetic antiferromagnetic (SAFM) effect on the magnetization of the pinned ferromagnetic (FM) layer and the influence of the barrier material impurity on the TMR performance.
- 3) The noise analysis of MTJs will be developed to explore the signal and noise aspects of MTJs for sensing applications. It aims at studying the noise sources of MTJs as well as the influence of the barrier defects on the MTJ outputs.
- 4) Based on the fabrication methodology presented in this thesis, MTJ sensors will be fabricated and measured to validate the simulation results. Novel materials for the barrier layer and the FM layer as well as new structures (e.g., multiple barrier layers) will be explored to achieve higher TMR and better magnetic field sensitivity. Methods for the measurements of the MTJ sensors will be determined so as to achieve the magnetic and electric properties of the MTJ sensors.
- 5) The fabricated MTJ sensors will be implemented for real-world sensing applications to improve the production quality.

Bibliography

- [1] R. Feynman, R. Leighton, and M. Sands, *The Feynman Lectures on Physics*, vol. 1, USA, Addison-Wesley, 1963.
- [2] W. Thomson, "On the Electro-Dynamic Qualities of Metals:--Effects of Magnetization on the Electric Conductivity of Nickel and of Iron", *Proceedings of the Royal Society of London*, vol. 8, pp. 546-550, 1857.
- [3] Western Digital. (1999). *AMR and GMR Heads Increase Hard Drive Capacity in Western Digital Drives* [Online]. Available: <http://www.wdc.com/wdproducts/library/other/2579-850121.pdf>.
- [4] Nobelprize.org. (2012). *The Nobel Prize in Physics 2007* [Online]. Available: http://www.nobelprize.org/nobel_prizes/physics/laureates/2007/.
- [5] M. Julliere, "Tunneling between ferromagnetic films," *Physic Letters A*, vol. 54, no. 8, pp. 225-226, 1975.
- [6] W. H. Butler, X. G. Zhang, and T. C. Schulthess, "Spin-dependent tunneling conductance of Fe/MgO/Fe sandwiches," *Physical Review B*, vol.63, no. 5, pp. 054416-054428, 2001.
- [7] J. Mathon and A. Umerski, "Theory of tunneling magnetoresistance of an epitaxial Fe/ MgO/ Fe(001) junction," *Physical Review B*, vol. 63, no. 22, pp. 220403-220407, 2001.
- [8] S. Ikeda, J. Hayakawa, Y. Ashizawa, Y. M. Lee, K. Miura, H. Hasegawa, M. Tsunoda, F. Matsukura, and H. Ohno, "Tunnel magnetoresistance of 604% at 300 K by suppression of Ta diffusion in CoFeB/MgO/CoFeB pseudo-spin-valves annealed

- at high temperature," *Applied Physics Letters*, vol. 93, no. 8, pp. 082508-082511, 2008.
- [9] M. Fecioru-Morariu, G. Guntherodt, M. Ruhrig, A. Lamperti and B. Tanner, "Exchange coupling between an amorphous ferromagnet and a crystalline antiferromagnet," *Journal of Applied Physics*, vol. 102, no. 5, pp. 053911-053917, 2007.
- [10] S. Parkin, X. Jiang, C. Kaiser, A. Panchula, K. Roche, and M. Samant, "Magnetically engineered spintronic sensors and memory," *Proceedings of the IEEE*, vol. 91, no. 5, pp. 661-680, 2003.
- [11] N. F. Mott, "The electrical conductivity of transition metals," *Proceedings of the Royal Society*, vol. 153, pp. 700-717, 1935.
- [12] R. Meservey and P.M. Tedrow, "Spin-polarized electron tunneling," *Physics Report*, vol. 238, pp. 173-243, 1994.
- [13] J. B. Kammerer, L. Hébrard, M. Hehn, F. Braun, P. Alnot, and A. Schuhl, "Compact modeling of a magnetic tunnel junction using VHDL-AMS: Computer aided design of a two-axis magnetometer," *Proceedings of IEEE Sensors*, vol. 3, pp. 1558-1561, 2004.
- [14] J. Slonczewski, "Conductance and exchange coupling of two ferromagnets separated by a tunneling barrier," *Physical Review B*, vol. 39, no. 10, pp. 6995-7002, 1989.
- [15] F. Li, Z. Li, M. Xiao, W. Xu, A. Hu, and J. Xiao, "Bias dependent tunneling in ferromagnetic junctions and inversion of the tunneling magnetoresistance from a quantum mechanical point of view," *Journal of Applied Physics*, vol. 95, no. 11, pp. 7243-7245, 2004.

- [16] J. G. Simmons, "Electric Tunnel Effect between Dissimilar Electrodes Separated by a Thin Insulating Film," *Journal of Applied Physics*, vol. 34, no. 9, pp. 2581-2591, 1963.
- [17] J.C. Fisher and I. Giaever, "Tunneling Through Thin Insulating Layers," *Journal of Applied Physics*, vol. 32, no. 2, pp. 172-178, 1961.
- [18] W. Brinkman, R. Dynes, and J. Rowell, "Tunneling conductance of asymmetrical barrier," *Journal of Applied Physics*, vol. 41, no. 5, pp. 1915-1921, 1970.
- [19] Y. Lu, X. W. Li, G. Xiao, R. A. Altman, W. J. Gallagher, A. Marley, K. Roche and S. Parkin, "Bias Voltage and Temperature Dependence of Magnetotunneling Effect," *Journal of Applied Physics*, vol. 83, no. 11, pp. 6515-6517, 1998.
- [20] J. Dubowik, B. Szymanski, F. Stobiecki, and K. Roll, "Interlayer exchange coupling across Cu/Ti/Cu spacer layer," *Physical Status Solidi (a)*, vol. 196, no. 1, pp. 86-89, 2003.
- [21] B. D. Schrag, A. Anguelouch, S. Ingvarsson, G. Xiao, Y. Lu, P. L. Trouilloud, A. Gupta, R. A. Wanner, W. J. Gallagher, P. M. Rice, and S. S. P. Parkin, "Néel "orange-peel" coupling in magnetic tunneling junction devices," *Applied Physics Letters*, vol. 77, no. 15, pp. 2373-2376, 2000.
- [22] M. Hehn, D. Lacour, F. Montaigne, J. Briones, R. Belkhou, S. El Moussaoui, F. Maccherozzi, and N. Rougemaille, "360° domain wall generation in the soft layer of magnetic tunnel junction," *Applied Physics Letters*, vol. 92, no. 7, pp. 072501-072504, 2008.

- [23] A. Smith, K. K. Nielsen, D. V. Christensen, C. R. H. Bahl, R. Bjork, and J. Hattel, "The demagnetizing field of a nonuniform rectangular prism," *Journal of Applied Physics*, vol. 107, no. 10, pp. 103910-103918, 2010.
- [24] D. X. Chen, E. Pardo, and A. Sanchez, "Demagnetizing factors of rectangular prisms and ellipsoids," *IEEE Transactions on Magnetics*, vol. 38, no. 4, pp. 1742-1752, 2002.
- [25] A. Aharoni, "Demagnetizing factors for rectangular ferromagnetic prisms," *Journal of Applied Physics*, vol. 83, no. 6, pp. 3432-3435, 1998.
- [26] M. Madec, J.-B. Kammerer, and L. Hébrard, "Compact modeling of a magnetic tunnel junction—Part I: Dynamic Magnetization Model," *IEEE Transactions on Electron Devices*, vol. 57, no. 6, pp. 1416-1424, 2010.
- [27] H. B. Ren and J. P. Wang, "Angle effect on the estimation of exchange coupling constant J for antiferromagnetically coupled medium," *Journal of Applied Physics*, vol. 93, no. 12, pp. 9875-9880, 2003.
- [28] T. L. Gilbert, "A phenomenological theory of damping in ferromagnetic materials," *IEEE Transactions on Magnetics*, vol. 40, no. 6, pp. 3443-3449, 2004.
- [29] E. du Trémolet de Lacheisserie, D. Gignoux, and M. Schlenker, *Magnetism: Fundamentals*. Berlin, Germany: Springer-Verlag, 2005.
- [30] E. P. Sajitha, J. Walowski, D. Watanabe, S. Mizukami, W. Feng, H. Naganuma, M. Oogane, Y. Ando, and T. Miyazaki, "Magnetization Dynamics in CoFeB Buffered Perpendicularly Magnetized Co/Pd Multilayer," *IEEE Transactions on Magnetics*, vol. 46, no.6, pp.2056-2059, 2010.

- [31] S. Zhang and Z. Li, "Roles of nonequilibrium conduction electrons on the magnetization dynamics of ferromagnets," *Physical Review Letters*, vol. 93, no. 12, pp. 127204-127206, 2004.
- [32] J. A. Katine, F. J. Albert, R. A. Buhrman, E. B. Myers, and D. C. Ralph, "Current-Driven Magnetization Reversal and Spin-Wave Excitations in Co/Cu/Co Pillars," *Physical Review Letters*, vol. 84, no. 14, pp. 3149-3152, 2000.
- [33] Netgen. (2009). *Automatic Mesh Generator* [Online]. Available: <http://www.hpfem.jku.at/netgen>.
- [34] M. Yoshikawa, T. Kai, M. Amano, E. Kitagawa, T. Nagase, M. Nakayama, S. Takahashi, T. Ueda, T. Kishi, K. Tsuchida, S. Ikegawa, Y. Asao, H. Yoda¹, Y. Fukuzumi, K. Nagahara, H. Numata, H. Hada, N. Ishiwata, and S. Tahara, "Bit yield improvement by precise control of stray fields from SAF pinned layers for high-density MRAMs", *Journal of Applied Physics*, vol. 97, no. 10, pp. 10P508-10P511, 2005.
- [35] A. Girdhar, "MgO-Based Magnetic Tunnel Junctions: Supermagnetism and Micromagnetics," M. S. thesis, Brown Univ., Providence, RI, 2009.
- [36] S. Kobe, A. R. Ferchmin, *The Landolt-Börnstein Database*, SpringerMaterials, 2013.
- [37] S. V. Komogortsev, E. A. Denisova, R. S. Iskhakov, A. D. Balaev, L. A. Chekanova, Y. E. Kalinin, and A. V. Sitnikov, "Multilayer nanogranular films $(\text{Co}_{40}\text{Fe}_{40}\text{B}_{20})_{50}/\alpha\text{-Si:H}$ and $(\text{Co}_{40}\text{Fe}_{40}\text{B}_{20})_{50}/\text{SiO}_2$: Magnetic properties," *Journal of Applied Physics*, vol. 113, no. 17, pp. 17C105-17C105-3, 2013.

- [38]H. Kohlstedt, N. A. Pertsev, J. Rodríguez Contreras¹, and R. Waser, “Theoretical current-voltage characteristics of ferroelectric tunnel junctions,” *Physical Review B*, vol. 72, no. 12, pp. 125341-125351, 2005.
- [39]Cláudio Aquino dos Santos, “MgO MTJ sensors in Wheatstone bridge for magnetometer devices,” M. S. thesis, Instituto Superior Técnico, Lisboa, PT, 2010.
- [40]L. Chih-Ling, A. Devasahayam, M. Mao, J. Kools, P. Cox, K. Masaryk, D. Mahenthiran, and J. Munson, “Seed layer characterization for PtMn bottom spin-filter spin valves”, *Journal of Applied Physics*, vol. 93, no. 10, pp. 8406-8409, 2003.
- [41]L. Ritchie, X. Liu, S. Ingvarsson, G. Xiao, J. Du, and J. Q. Xiao, “Magnetic exchange bias enhancement through seed layer variation in FeMn/NiFe layered structures,” *Journal of Magnetism and Magnetic Materials*, vol. 247, no. 2, pp. 187-190, 2002.
- [42]P. Wiśniowski, T. Stobiecki, J. Kanak, G. Reiss, and H. Brückl, “Influence of buffer layer texture on magnetic and electrical properties of IrMn spin valve magnetic tunnel junctions”, *Journal of Applied Physics*, vol. 100, no. 1, pp. 013906-013913, 2006.
- [43]K. Nakamura, M. Kim, A. J. Freeman, L. Zhong, and J. Fernandez-de-Casto, "Magnetism and magnetic anisotropy in FM NiFe, AFM NiMn, and their interface," *IEEE Transactions on Magnetics*, vol. 36, no. 5, pp. 3269-3271, 2000.
- [44]J. P. Nozières, S. Jaren, Y. B. Zhang, A. Zeltser, K. Pentek, and V. S. Speriosu, “Blocking temperature distribution and long-term stability of in-valve structures with Mn-based antiferromagnets,” *Journal of Applied Physics*, vol. 87, no. 8, pp. 3920-3925, 2000.

- [45] G. Anderson, Y. Huai, and L. Miloslavsky, "Spin-Valve GMR Films Based on Antiferromagnetic NiMn", *MRS Proceedings*, vol. 562, no. 45, 1999.
- [46] W. Shen, "Ultra-sensitive MgO-based Magnetic Tunnel Junctions for Spintronic Immunoassay," Ph. D. dissertations, Dept. of Physics, Brown Univ., Providence, RI, 2007.
- [47] M. Yoshikawa, T. Kai, M. Amano, E. Kitagawa, T. Nagase, M. Nakayama, S. Takahashi, T. Ueda, T. Kishi, K. Tsuchida, S. Ikegawa, Y. Asao, H. Yoda, Y. Fukuzumi, K. Nagahara, H. Numata, H. Hada, N. Ishiwata, and S. Tahara, "Bit yield improvement by precise control of stray fields from SAF pinned layers for high-density MRAMs," *Journal of Applied Physics*, vol. 97, no. 10, pp. 508-511, 2005.
- [48] Y. M. Lee, J. Hayakawa, S. Ikeda, F. Matsukura, and H. Ohno, "Giant tunnel magnetoresistance and high annealing stability in CoFeB/MgO/CoFeB magnetic tunnel junctions with synthetic pinned layer," *Applied Physics Letters*, vol. 89, no. 4, pp. 042506-042509, 2006.
- [49] K. Tsunekawa, D. D. Djayaprawira, S. Yuasa, M. Nagai, H. Maehara, S. Yamagata, E. Okada, N. Watanabe, Y. Suzuki, and K. Ando, "Huge magnetoresistance and low junction resistance in magnetic tunnel junctions with crystalline MgO barrier", *IEEE Transactions on Magnetics*, vol. 42, no. 2, pp. 103-107, 2006.
- [50] W. H. Butler, "Tunneling magnetoresistance from a symmetry filtering effect," *Science and Technology of Advanced Materials*, vol. 9, no. 1, pp. 014106-014123, 2008.
- [51] E. Y. Tsymbal, *HANDBOOK OF SPIN TRANSPORT AND MAGNETISM*, Chapman and Hall/CRC, Lincoln, USA, 2011.

- [52] Carleton University's Microfabrication Facility. (2013). *Oxidation/Diffusion*.
 [Online]. Available: <http://www.doe.carleton.ca/facilities/fab/oxdiff.php>.
- [53] C. R. Raum, "THERMO-MECHANICALLY TUNABLE BRAGG GRATING FILTERS ON SILICON-ON-INSULATOR RIB WAVEGUIDE BRIDGES," Ph. D. dissertations, Elec. Dept., Carleton Univ., Ottawa, ON, 2010.
- [54] W. G. Wang, C. Ni, A. Rumaiz, Y. Wang, X. Fan, T. Moriyama¹, R. Cao, Q. Y. Wen, H. W. Zhang, and John Q. Xiao, "Real-time evolution of tunneling magnetoresistance during annealing in CoFeB/MgO/ CoFeB magnetic tunnel junctions," *Applied Physics Letters*, vol. 92, no. 15, pp. 152501-152504, 2008.
- [55] D. D. Djayaprawira, K. Tsunekawa¹, M. Nagai, H. Maehara, S. Yamagata, N. Watanabe, S. Yuasa, Y. Suzuki, and K. Ando, "230% room-temperature magnetoresistance in CoFeB/MgO/CoFeB magnetic tunnel junctions," *Applied Physics Letters*, vol. 86, no. 9, pp. 092502-091405, 2005.
- [56] J. Cao, J. Kanak, T. Stobiecki, P. Wisniowski, and P. P. Freitas, "Effect of Buffer Layer Texture on the Crystallization of CoFeB and on the Tunnel Magnetoresistance in MgO Based Magnetic Tunnel Junctions," *IEEE Transactions on Magnetics*, vol. 45, no 10, pp. 3464-3466, 2009.
- [57] S. Weinberg, *Dreams of a Final Theory*, London, Hutchinson Rasius, 1993.
- [58] M. McCaig, *Permanent magnets in theory and practice*, Pentech Press Ltd, 1977.
- [59] A. Zhang, Z. Cao, Q. Shen, X. Dou and Y. Chen, "Tunnelling coefficients across an arbitrary potential barrier," *Journal of Physics A: Mathematical and General*, vol. 33, no. 30, pp. 5449-5457, 2000.
- [60] J.L. Powell and B. Crasemann, *Quantum Mechanics*, Addison-Wesley, 1963.

- [61] M. Razavy, *Quantum Theory of Tunneling*, World Scientific, 2003.
- [62] M. Abramowitz and I. A. Stegun, *Handbook of Mathematical Functions with Formulas, Graphs, and Mathematical Tables*, New York: Dover, 1965.
- [63] M. E. Eames, "The Theory of Magnetic Tunnel Junctions," Ph.D. dissertation, Univ. of Exeter, Devon, UK, 2007.
- [64] F. Montaigne, M. Hehn, and A. Schuhl, "Tunnel barrier parameters and magnetoresistance in the parabolic band model," *Physical Review B*, vol. 64, no. 14, pp. 144402-144406, 2001.
- [65] F. Guinea, "Spin-flip scattering in magnetic junctions," *Physical Review B*, vol. 58, no. 14, pp. 9212-9216, 1998.
- [66] Carnegie Mellon Nanofabrication Facility. (2013). *Micro Magnetics SpinTherm 1000 Magnetic Thermal Annealing System*. [Online]. Available: <http://www.nanofab.ece.cmu.edu/equipment/machines/spintherm.html>.
- [67] National Institute of Standards and Technology. (2013). *NIST CNST NanoFab Equipment Specialty Tools*. [Online]. Available: http://www.cnst.nist.gov/nanofab/nanofab_equipment/specialty_tools.html.